ACS OMEGA

Article

Cite This: ACS Omega 2018, 3, 7046−7060

Continuous Hydrothermal Decarboxylation of Fatty Acids and Their Derivatives into Liquid Hydrocarbons Using Mo/Al_2O_3 Catalyst

Md Zakir Hossain,[†] Muhammad B. I. Chowdhury,[†] Anil Kumar Jhawar,[†] William Z. Xu,[†] Mark C. Biesinger,[‡] and Paul A. Charpentier*[,†]

[†]Department of Chemical and Biochemical Engineering, Western University, London, Ontario N6A 5B9, Canada

[‡]Manager, Research and Business Development, Surface Science, Western University, London, Ontario N6G 0J3, Canada

Supporting Information

ABSTRACT: In this study, we report a single-step continuous production of straight-chain liquid hydrocarbons from oleic acid and other fatty acid derivatives of interest including castor oil, frying oil, and palm oil using Mo, MgO, and Ni on Al_2O_3 as catalysts in subcritical water. Straight-chain hydrocarbons were obtained via decarboxylation and hydrogenation reactions with no added hydrogen. Mo/Al_2O_3 catalyst was found to exhibit a higher degree of decarboxylation (92%) and liquid yield (71%) compared to the other two examined catalysts (MgO/Al_2O_3, Ni/Al_2O_3) at the maximized conditions of 375 °C, 4 h of space time, and a volume ratio of 5:1 of water to oleic acid. The obtained liquid product has a similar density (0.85 kg/m^3 at 15.6 °C) and high heating value (44.7 MJ/kg) as commercial fuels including kerosene (0.78−0.82 kg/m^3 and 46.2 MJ/kg), jet fuel (0.78−0.84 kg/m^3 and 43.5 MJ/kg), and diesel fuel (0.80−0.96 kg/m^3 and 44.8 MJ/kg). The reaction conditions including temperature, volume ratio of water-to-feed, and space time were maximized for the Mo/Al_2O_3 catalyst. Characterization of the spent catalysts showed that a significant amount of amorphous carbon deposited on the catalyst could be removed by simple carbon burning in air with the catalyst recycled and reused.

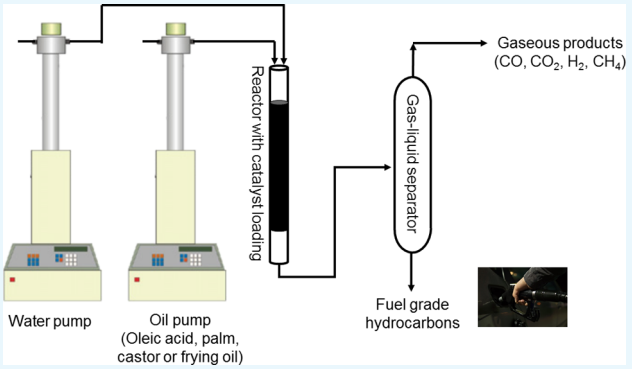

INTRODUCTION

Renewable resources are of increasing interest to produce fuel range hydrocarbons, especially liquid transportation fuels because of the limited reserves of petroleum fuel. Fats & oil (which mainly contain triglycerides and fatty acids) have been used as renewable feedstocks for producing transportation fuels such as biodiesel[1−4] or green diesel.[5−8] Nonedible resources (jatropha oil, algae, waste cooking oil, animal fats, tallow, etc.) are preferred as feedstocks over edible resources to avoid the food versus fuel issue. However, higher oxygen content and acidity of these feedstocks prevent them from being used directly as fuel because of their corrosive properties and higher viscosity compared to fossil fuels.[9] To lower the oxygen content, deoxygenation is an efficient upgrading pathway to produce diesel range liquid hydrocarbons to minimize any issues related to engine compatibility. Liquid hydrocarbon formed via the deoxygenation process can obtain larger cetane numbers (85 to 99) compared to petroleum diesel (45 to 55).[10]

Decarboxylation is a cost-effective deoxygenation process for liquid hydrocarbon production as it requires less/no hydrogen compared to other processes such as hydrodeoxygenation. The decarboxylation process requires a catalyst to produce higher yield/selectivity of liquid hydrocarbons. Catalytic decarboxylation of lipid-based feedstocks in water, that is, hydrothermal processing, is a promising pathway for producing liquid hydrocarbons.[6,8,11] Water has several unique properties at its subcritical conditions (200−375 °C, 5−20 MPa), including a lower dielectric constant, which enhances solubility of the lipid-based feedstocks.[12] The relatively large ionization constant of subcritical water makes a highly reactive reaction media by minimizing mass-transfer limitations.[12] Water is also a good solvent for lipid feedstocks containing a large moisture content (algal biomass, sewage sludge, or fish and animal fat processing residues).[13−15]

Most catalytic processes for decarboxylation have used noble metal catalysts and high-pressure and external sources of hydrogen or carbon dioxide to enhance the feedstock conversion and liquid product yield/selectivity.[4,6,16−23] Yang et al.[19] studied decarboxylation of oleic acid (OA) using Pt/zeolite 5A and Pt/ZIF-67/zeolite 5A catalysts in the presence of high-pressure (20 bar) hydrogen to obtain 98.7% conversion of OA with 72.6 and 81.5% selectivity of heptadecane, respectively. In the presence of a CO_2 (20 bar) atmosphere, decarboxylation of palmitic and lauric acids using this catalyst system gave 95% conversion of both fatty acids with 91.7 and

Received: March 24, 2018
Accepted: June 15, 2018
Published: June 28, 2018

DOI: 10.1021/acsomega.8b00562
ACS Omega 2018, 3, 7046−7060

93.5% selectivity of pentadecane and undecane, respectively.[18] Mäki-Arvela et al.[21] conducted tall oil fatty acid deoxygenation using a Pd/C catalyst with 1% H_2 balanced with argon (17 bar) to enhance the selectivity and conversion of heptadecane. The main shortcoming of noble metal catalysts is their limited availability and high cost. Fu et al.[8] and Hossain et al.[5,24] showed that hydrothermal decarboxylation did not require external hydrogen, with the required hydrogen to saturate the product being produced in situ by the water−gas shift reaction. Water is well known to participate as a coreactant with CO in the water−gas shift reaction under hydrothermal conditions, with CO being produced via decarbonylation or thermal cracking of the fatty acids.[5,24]

On the other hand, sulfided catalysts (e.g., sulfided CoMo or NiMo oxides) are also used for decarboxylation,[25,26] which are comparatively cheaper than noble metal catalysts, but leaching of sulfur may deactivate the catalytic activity and contaminate the products, requiring an additional step for sulfur recovery.[27,28] Besides the noble or sulfided catalysts, researchers reported non-sulfided catalysts for decarboxylation. Morgan et al.[29] reported the production of C5 to C17 hydrocarbons from triolein and soybean oil using a nickel-supported catalyst. Wu et al.[30] obtained over 80% selectivity of heptadecane using a nickel-supported catalyst during stearic acid decarboxylation. Na et al.[31] reported more than 98% conversion and less than 1 wt % of oxygen content in the product mixture during decarboxylation of OA using a supported MgO catalyst. Content of hydrocarbon (81.1%) and a low moisture content of biofuel from carinata oil were reported by Zhao et al.[32] using an Mo−Zn/Al_2O_3 catalyst. Most of these reported studies were conducted in batch, whereas the reaction chemistry in continuous operation (important for commercialization) is not well-known. Moreover, Hengst et al.[33] reported that acidic catalysts are preferable for enhancing the decarboxylation chemistry. However, they used noble metal (Pd) on different supports. In this study, we introduced Mo as a low-cost acidic catalyst for decarboxylation for the first time. For comparison purposes, Ni and MgO were used as reference catalysts.

The scope of this work is toward the continuous hydrothermal decarboxylation of OA as a model compound, while also examining other fatty acid derivatives including castor oil, frying oil, and palm oil. A current challenge for the continuous decarboxylation process is to develop low-cost stable catalysts. Moreover, the effect on the catalyst due to the exposure of the harsh sub or near supercritical water is poorly reported.

Here, we synthesize molybdenum (Mo)-, MgO-, and Ni-loaded alumina (γ-Al_2O_3) catalysts and investigate them for OA decarboxylation. The best catalyst was chosen among these three based on the degree of decarboxylation of OA. With the best catalyst determined, the effects of process parameters including temperature, space time, and water-to-OA (v/v) ratio were studied in hydrothermal media (subcritical water) using a continuous fixed-bed catalytic reactor. The catalytic activities for decarboxylation of several fatty acid derivatives including castor oil, frying oil, palm oil were then investigated. Characterization of fresh and spent catalysts was conducted using several physicochemical techniques including N_2-physisorption [Brunauer−Emmett−Teller (BET) surface area and Barrett−Joyner−Halenda (BJH) pore size distribution], NH_3 temperature-programmed desorption (NH_3-TPD), X-ray diffraction (XRD), H_2 temperature-programmed reduction (H_2-TPR), CO pulse chemisorption, X-ray photoelectron spectroscopy (XPS), transmission electron microscopy (TEM), scanning electron microscopy (SEM), and energy dispersive X-ray spectroscopy (EDXS).

RESULTS AND DISCUSSION

Characterization of Fresh Catalysts. Mo, MgO, and Ni catalysts are extensively used for decarboxylation of lipid-based feedstocks[30−32,34−38] and of interest for this study. The first part of this study investigated the production of three metals on an alumina support using an incipient impregnation method, with a target of 10 wt % metal on alumina. EDXS analysis was performed to quantify the actual metal loading for catalyst synthesis, with the results shown in Table 1 and Figure S1. The actual loading of Mo and Ni was found to be 10.1 and 10.0 wt %, respectively. The wt % of Mo (9.10%) was also confirmed by XPS analysis. Because EDXS cannot determine the oxidation state of any metal, the actual loading of MgO was calculated from the weight difference between the catalyst sample after calcination and before loading, that is, 9.76 wt %. However, no elemental S was detected for the 10 wt % MgO−Al_2O_3 catalyst during EDXS analysis.

Table 1. Elemental Compositions of Fresh 10 wt % Mo−Al_2O_3 and 10 wt % Ni−Al_2O_3 Catalysts

catalysts	Al (wt %)	O (wt %)	Mo (wt %)	Ni (wt %)
10 wt % Mo−Al_2O_3	24.7	65.2	10.1	
10 wt % Ni−Al_2O_3	25.4	64.6		10

Textural properties of any catalyst are important parameters to measure its catalytic activity. N_2 adsorption−desorption isotherms and pore size distributions are displayed in Figure S2 and their corresponding pore properties are shown in Table 2.

Table 2. Summary of BET Surface Area, Pore Volume, and Pore Size of Fresh and Spent Catalysts

sample name	fresh/spent	BET surface area (m^2/g)	pore volume (cm^3/g)	average pore size (nm)
Al_2O_3	fresh	179	0.50	11.1
10 wt % Mo−Al_2O_3	fresh	160	0.44	9.6
	spent	78	0.23	10.2
10 wt % MgO−Al_2O_3	fresh	163	0.45	10.5
	spent	99	0.22	18.4
10 wt % Ni−Al_2O_3	fresh	158	0.45	10.5
	spent	111	0.28	10.0

The isotherms of Al_2O_3 in Figure S2(i)a, fresh 10 wt % Mo−Al_2O_3 in Figure S2(i)b, 10 wt % MgO−Al_2O_3 in Figure S2(i)c, and 10 wt % Ni−Al_2O_3 in Figure S2(i)d showed a typical type IV isotherm with a H1-type hysteresis loop. This indicates that all fresh catalysts possessed a mesoporous structure.[39,40] Mesoporosity of the prepared catalysts was confirmed by pore size distributions in Figure S2(ii). As presented in Table 2, the BET surface area and pore volume of all fresh catalysts are lower than those of the support, indicating that Mo, MgO, and Ni loadings partially blocked Al_2O_3 pores during the catalyst preparation step (impregnation method). BET surface area and pore volume of the three synthesized catalysts are slightly different from each other, which follows the order: 10

DOI: 10.1021/acsomega.8b00562
ACS Omega 2018, 3, 7046−7060

wt % $MgOAl_2O_3$ > 10 wt % $Mo-Al_2O_3$ > 10 wt % $Ni-Al_2O_3$. The average pore diameters of all fresh catalysts are analogous to each other and slightly lower than that of the Al_2O_3 support.

Decarboxylation of free fatty acids is known to largely depend on the acidity of the catalyst. For example, Hengst et al.[33] found enhanced deoxygenation activity of free fatty acids for diesel fuel production using an acidic catalyst (Pd/Pural SB1-derived Al_2O_3). The NH_3 TPD of fresh catalysts is shown in Figure 1 to determine the acidity of the investigated

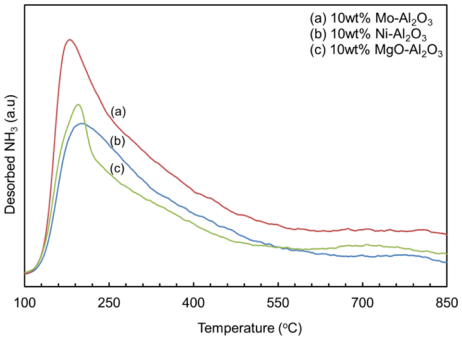

Figure 1. NH_3 TPD of fresh catalysts.

catalysts. The peak at around 100−350 °C is assigned to the Lewis acid sites and the peak at 500 °C represents the Bronsted acid sites, respectively, in the TPD profiles.[41−43] The NH_3 TPD profiles show that all catalysts contain mostly Lewis acid sites. The total amounts of ammonia desorbed by $Mo-Al_2O_3$, $Ni-Al_2O_3$, and $MgO-Al_2O_3$ are 33.5, 25, and 24.3 mL STP/g. The value of NH_3 uptake indicates that the overall acidity of the $Mo-Al_2O_3$ catalyst is comparatively higher than that of the $Ni-Al_2O_3$ and $MgO-Al_2O_3$ catalysts.

Crystallinity of a metal-supported catalyst is usually measured by XRD. Figure 2(i) shows the XRD patterns of all fresh catalysts with support. Pure γ-Al_2O_3 phases at 2θ = 35.2, 47.2, and 67.6° are found in Figure 2(i)a.[38] Mostly, MoO_2 phases were found in the XRD pattern of fresh 10 wt % $Mo-Al_2O_3$ catalyst [Figure 2(i)b], which implies that Mo is a hard to reduce metal, even using a reduction temperature of 950 °C. Very weak reflections of pure Mo are observed at 2θ = 42 and 61°. Fresh 10 wt % $MgO-Al_2O_3$ and 10 wt % $Ni-Al_2O_3$ catalysts show mainly $MgAl_2O_4$ and $NiAl_2O_4$ phases, which indicates that all MgO and Ni particles react with Al_2O_3 to form $MgAl_2O_4$ and $NiAl_2O_4$, respectively [Figure 2(i)d,f]. Spinel $MgAl_2O_4$ phase was found at 2θ = 37.1, 45.3, and 66.1°. Spinel $NiAl_2O_4$ phase was found at 2θ = 37, 45, and 66°. No XRD peaks of MgO and Ni were found for the fresh catalysts, which may be due to the overlapping by reflections of $MgAl_2O_4$ and $NiAl_2O_4$ peaks or enhanced MgO or Ni dispersion on the catalyst surface.[44,45] Higher temperature for reduction or calcination enhances the formation of $MgAl_2O_4$ and $NiAl_2O_4$.[46] No $MgSO_4$ or S peaks were found in fresh 10 wt % $MgO-Al_2O_3$ catalyst as $MgSO_4 \cdot 7H_2O$ was used as the MgO precursor. S usually shows sharp peaks between 15 and 60°.[47] The sharp peak intensity of fresh 10 wt % $Ni-Al_2O_3$ catalyst compared to fresh 10 wt % $MgO-Al_2O_3$ and 10 wt % $Ni-Al_2O_3$ catalysts indicates the smaller metal particle phases present on the surface. Moreover, no reflections for θ-Al_2O_3 (25.6 and 43.3°) or α-Al_2O_3 (31.2 and 36.6°) were evident on the reduced catalysts. This indicates that phase changes of Al_2O_3 were not enhanced by the chosen reduction/calcination temperature.

H_2-TPR experiments were conducted to determine the optimum reduction temperature of the investigated catalysts. H_2-TPR profiles of fresh catalysts are shown in Figure 2(ii). Four reduction peaks are observed in the TPR profile of fresh 10 wt % $Mo-Al_2O_3$ at 475, 666, 925, and 1065 °C, respectively. It has been reported that Mo species reduction is a two-step process such as MoO_3 to MoO_2 and then MoO_2 to Mo.[48] Different reduction temperatures obtained in the TPR profile indicate the formation of different Mo species. It was previously reported that four types of Mo phases were formed during the reduction of Mo-based catalyst. Two forms of Mo species were reported by Ma et al.[49] One was polynuclear (located on the external surface of the support), either in a square-pyramidal coordination as MoO_x form or in an octahedral coordination as MoO_3 crystallite form. The second one was related to Al atoms in the lattice channel of support. The reduction peak at 475 °C of fresh 10 wt % $Mo-Al_2O_3$ is ascribed to the reduction of MoO_3 to MoO_2.[50] The strong peak assigned to 1065 °C indicates further reduction of MoO_2 to form metallic Mo.[51] The reduction peaks at 666 and 925 °C may be ascribed to the initial and the further reduction of the aggregative MoO_3 species.[48]

Fresh 10 wt % $MgO-Al_2O_3$ catalyst shows its only reduction peak at 475 °C, which represents the reduction of $MgAl_2O_4$. Usually two major reduction peaks at 250−350 and 600 −850 °C are observed for $Ni-Al_2O_3$ catalyst, corresponding to the easily reducible NiO and hard to reduce NiO, respectively.[52] Because there is no peak observed around 250−350 °C in this study, all NiO reacts with Al_2O_3 to form $NiAl_2O_4$. The

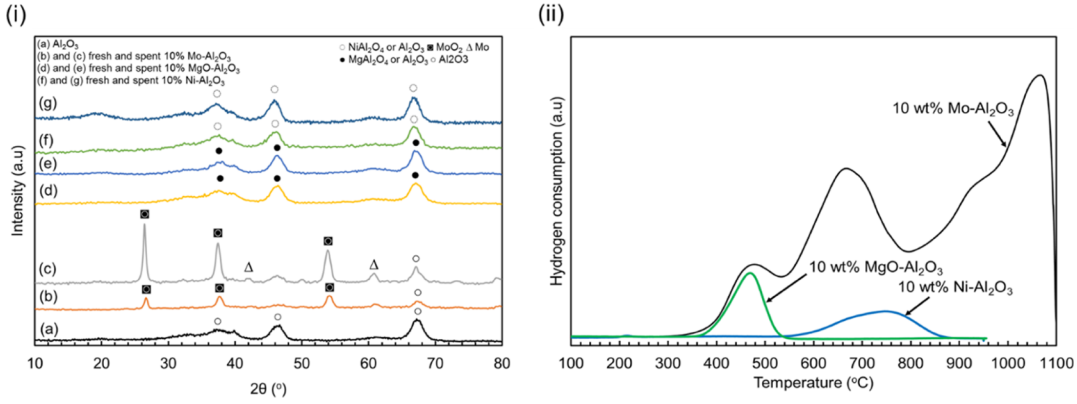

Figure 2. (i) XRD patterns of fresh and spent catalysts and (ii) TPR profiles of fresh catalysts.

DOI: 10.1021/acsomega.8b00562
ACS Omega 2018, 3, 7046−7060

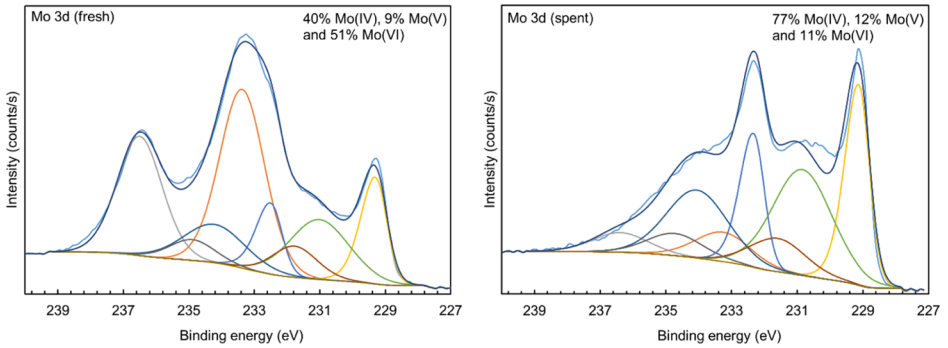

Figure 3. XPS high-resolution spectra of Mo (3d) for 10 wt % Mo/Al_2O_3 catalyst (detail peak assignment shown in Tables S1 and S7).

Table 3. CO Pulse Chemisorption Data of Fresh and Spent Catalysts

sample	fresh/spent	% metal dispersion	metallic surface area (m^2/g sample)	metallic surface area (m^2/g metal)	active particle diameter (nm)
10 wt % $Mo-Al_2O_3$	fresh	2.49	1.34	9.81	10.1
	spent	1.68	0.74	6.11	90.7
10 wt % $Ni-Al_2O_3$	fresh	1.94	0.81	6.74	95.8
	spent	0.45	0.32	3.05	200.3

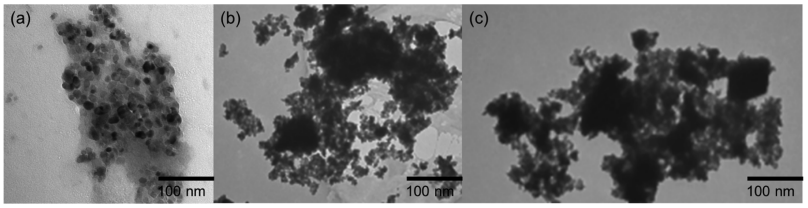

Figure 4. TEM images of fresh catalysts: (a) 10 wt % $Mo-Al_2O_3$; (b) 10 wt % $Ni-Al_2O_3$; and (c) 10 wt % $MgO-Al_2O_3$.

reduction peak of $NiAl_2O_4$ was observed at 750 °C for the fresh 10 wt % $Ni-Al_2O_3$. Reducibility of nickel catalysts largely depends on the wt % of nickel, calcination or reduction temperature, and the interaction between the metal and support.[53] Calcination or reduction at high temperature increases the metal−support interaction and the formation of $NiAl_2O_4$, which results in greater difficulty of nickel catalysts in reduction.

The metal−support interaction and the ease of reduction are determined from both the peak width and the reduction temperature. The wide peak represents a strong metal−support interaction and the higher temperature for reduction indicates a hard to reduce metal. It is observed from the TPR-H_2 profile that both fresh 10 wt % $Mo-Al_2O_3$ and 10 wt % $Ni-Al_2O_3$ were reduced at higher temperature compared to fresh 10 wt % $MgO-Al_2O_3$ catalyst. Comparing the fresh Mo- and Ni-based catalysts, the Mo catalyst was reduced at higher temperatures. However, the TPR-H_2 peaks for the MgO catalyst are comparatively narrower than those for the other two catalysts, indicating a weak interaction of MgO with Al_2O_3. The H_2-TPR results are consistent with the XRD results.

For a more detailed investigation of the surface structure, XPS spectra of the fresh 10 wt % $Mo-Al_2O_3$ are presented in Figure 3. The spectra were curve-fit using the screened and unscreened peak-fitting parameters [peak positions, full width at half-maximum (fwhm), and area ratios] for Mo(IV) as outlined by Scanlon et al.[54] The parameters obtained for fresh 10 wt % $Mo-Al_2O_3$ catalyst are provided in Table S1. An Mo $3d_{5/2}$−Mo $3d_{3/2}$ spin−orbit double for Mo(VI) was constrained to have an area ratio of 3:2, equal fwhms, a doublet spacing of 3.13 eV, and an Mo $3d_{5/2}$ peak position ranging from 232.2 to 232.6 eV. Peak fitting showed that a small component attributable to Mo(V) was also present. As such, a spin−orbit doublet, constrained to have a similar fwhm as that for the Mo(VI) component, was added with an Mo $3d_{5/2}$ peak position ranging from 231.6 to 231.9 eV.[55,56] It should be noted that the presence of the component attributed to Mo(V) in this fitting may be due to some portion of the Mo(IV) unscreened peak structure not accounted for by Scanlon et al.[54] fitting, possibly due to spectrometer differences. Mo(V) may also be present because of the X-ray reduction of MoO_3 during the analysis.[57]

Percent metal dispersion is an important parameter for a metal-supported catalyst, which enhances greatly the catalytic reaction. Pulse chemisorption experiments were conducted to quantify the % metal dispersion, the active metal surface area, and the active particle size of metal crystals on the alumina surface. Table 3 shows the CO pulse chemisorption data for 10 wt % $Mo-Al_2O_3$ and 10 wt % $Ni-Al_2O_3$ catalysts. Metal dispersion (2.49%) was found for fresh 10 wt % $Mo-Al_2O_3$ catalyst, whereas the value is smaller for fresh10 wt % $Ni-Al_2O_3$ catalyst. Higher metallic surface area per gram of sample and per gram of metal were also obtained for fresh 10 wt % $MgO-Al_2O_3$ catalysts compared to fresh 10 wt % $Ni-Al_2O_3$. Smaller active metal particle size was observed in fresh 10 wt % $Mo-Al_2O_3$ catalyst. The obtained larger metal particle size from the Ni-based catalyst is attributed to the lower dispersion and metallic surface area.

The morphology of the fresh catalysts was observed using TEM. The 10 wt % $Mo-Al_2O_3$ catalyst shows small metal particles distributed over the surface, whereas the 10 wt % $Ni-Al_2O_3$ and 10 wt % $MgO-Al_2O_3$ catalysts have larger metal

DOI: 10.1021/acsomega.8b00562
ACS Omega 2018, 3, 7046−7060

particles on their surfaces (Figure 4). Small Mo particles improve the % metal dispersion and reduce the active particle diameter, whereas the larger metal particles of Ni and MgO catalysts reduce the % metal dispersion. Smaller particle size provides more active sites for the decarboxylation reaction compared to larger particle size. The TEM results are consistent with the CO pulse chemisorption results.

Decarboxylation of OA. *Screening of Decarboxylation Catalyst.* The initial experiments compared the catalytic activities for OA decarboxylation in a continuous flow reactor using 10 wt % loading of Ni, Mo, and MgO on γ-Al_2O_3 at 375 °C, space time of 4 h, and ratio (v/v) of water-to-OA = 5:1 using 5 g of catalyst. Figure 5 depicts the attenuated total

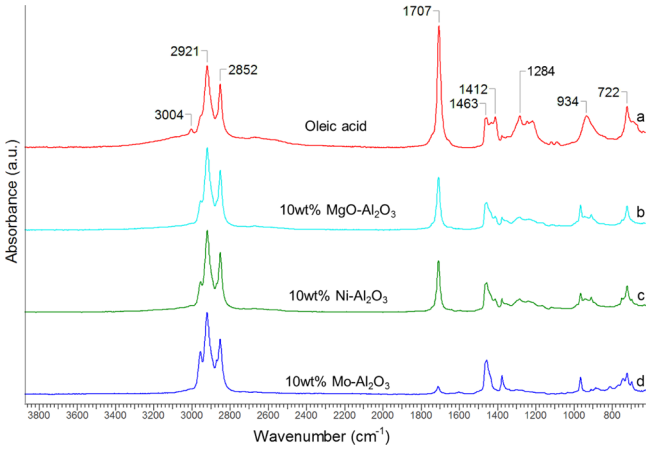

Figure 5. ATR−FTIR spectra of (a) OA and the formed products using different catalysts such as (b) 10 wt % MgO−Al_2O_3, (c) 10 wt % Ni−Al_2O_3, and (d) 10 wt % Mo−Al_2O_3.

reflection−Fourier transform infrared (ATR−FTIR) spectra of the decarboxylated liquid products with the degree of decarboxylation being calculated by eq 1. The results show that the degree of decarboxylation of OA varied strongly using the investigated catalysts, being 67, 65, and 92% using a 10 wt % MgO−Al_2O_3, 10 wt % Ni−Al_2O_3, and 10 wt % Mo−Al_2O_3 catalyst, respectively. The obtained liquid and gaseous product yields using these three catalysts are liquid yield = 65, 30, and 71% and gaseous yields are 35, 70, and 29%, for the 10 wt % MgO−Al_2O_3, 10 wt % Ni−Al_2O_3, and 10 wt % Mo−Al_2O_3, respectively. The low liquid and high gaseous product yields indicate that the 10 wt % Ni−Al_2O_3 catalyst is primarily a gasification catalyst, consistent with our previous work on supercritical water gasification.[58−61]

Although all catalysts have similar BET surface area, higher acidity and metal dispersion of 10 wt % Mo−Al_2O_3 catalysts are favored for a higher degree of decarboxylation (92%). Higher metal dispersion, metallic surface area, and smaller metal particle sizes of the 10 wt % Mo−Al_2O_3 catalyst provide more active sites for decarboxylation of fatty acids. Hengst et al.[33] showed that an acidic catalyst enhanced the deoxygenation and cracking of free fatty acids into diesel fuels.

Because the molar mass of Mo (96 g) is higher than those of Ni (58.7 g) and MgO (40.3 g), the molar percentages of Ni and MgO in 10 wt % Ni−Al_2O_3 and 10 wt % MgO−Al_2O_3 catalysts are much higher than that of Mo in the 10 wt % Mo−Al_2O_3 catalyst at the same loading wt %. Hence, the catalytic performance of the 10 wt % Mo−Al_2O_3 catalyst is much better than the other two.

The gaseous products CO and CO_2 found in the product streams are compared in Figure S3. The Ni−Al_2O_3 and MgO−Al_2O_3 catalysts gave a higher yield of CO compared to CO_2, whereas the Mo−Al_2O_3 catalyst provided a high yield of CO_2 compared to CO. This indicates that the Mo-based catalyst dominates the decarboxylation of OA under the chosen reaction conditions at which the best catalyst was determined for this study. Significant amounts of H_2 and CH_4 and lighter fractions of hydrocarbons (C_2 to C_4) were found using the Ni−Al_2O_3 catalyst (data not shown). On the basis of these initial ATR−FTIR and gas chromatography−thermal conductivity detection (GC-TCD) results, the 10 wt % Mo/Al_2O_3 catalyst was chosen for the subsequent parametric study examining the experimental conditions.

Table S2 shows carbon balance using 10 wt % MgO/Al_2O_3, 10 wt % Ni/Al_2O_3, and 10 wt % Mo/Al_2O_3 catalysts for the decarboxylation of OA at 375 °C, space time of 4 h, and water-to-OA (v/v) ratio of 5:1 using 5 g of catalyst. The carbon balance in all cases is found to be 97 to 99%.

Effect of Reaction Parameters on Degree of Decarboxylation. Reaction parameters including temperature, water-to-OA (v/v) ratio, and space time (τ) are the three most important parameters for a continuous hydrothermal decarboxylation reaction. ATR−FTIR spectra of the decarboxylated liquid products obtained under different experimental conditions (T = 325 to 400 °C, ratio (v/v) of water to OA = 2:1 to 5:1 & space time = 0.5 to 4 h) using 5 g of 10 wt % Mo−Al_2O_3 catalyst are presented in Figure 6, whereas Figure

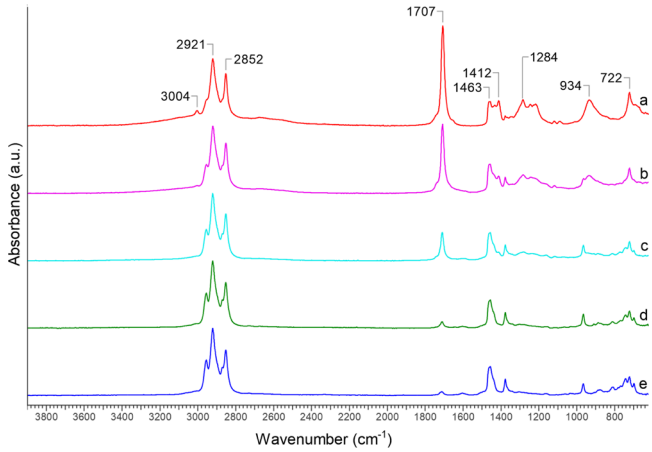

Figure 6. ATR−FTIR spectra of (a) OA and the products formed using water-to-OA (v/v) ratio of 5:1 and 4 h of reaction time at (b) 325, (c) 350, (d) 375, and (e) 400 °C.

S4 shows the corresponding degree of decarboxylation. The results show that increasing temperature from 325 to 375 °C enhanced the percent decarboxylation (from 55 to 92%) (Figure S4a). Further increasing of temperature from 375 to 400 °C improved the degree of decarboxylation by only 0.3%. The results show that the degree of decarboxylation of OA is less sensitive to temperature above 375 °C. Therefore, the maximized temperature chosen for this study was 375 °C.

The effects of process parameters of water-to-OA ratio (v/v) and space time at 375 °C on the formed decarboxylated products are presented in Figure 7. Figure S4b,c shows their corresponding degree of decarboxylation. The results indicate that increasing the ratio (v/v) of water-to-OA from 2:1 to 5:1 and space time from 0.5 to 4 h enhanced the percent

DOI: 10.1021/acsomega.8b00562
ACS Omega 2018, 3, 7046−7060

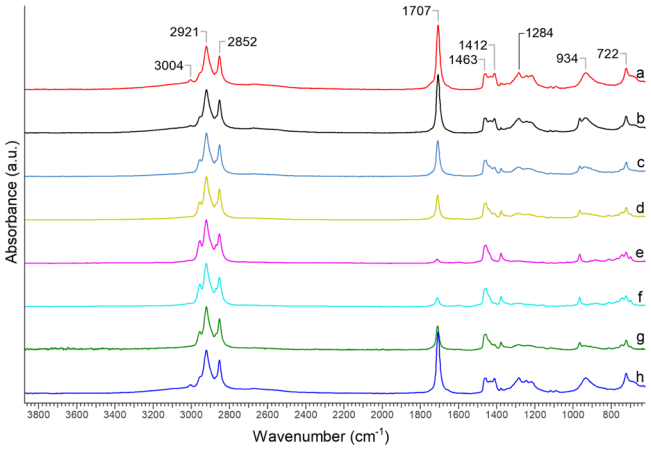

Figure 7. ATR−FTIR spectra of (a) OA and the products formed at 375 °C for different reaction times using different ratios of water-to-OA (v/v): (b) 0.5 h and ratio of 5:1; (c) 1 h and ratio of 5:1; (d) 2 h and ratio of 5:1; (e) 4 h and ratio of 5:1; (f) 4 h and ratio of 4:1; (g) 4 h and ratio of 3:1; and (h) 4 h and ratio of 2:1.

decarboxylation. The maximum degree of decarboxylation (92%) was obtained at 375 °C, ratio (v/v) of water-to-OA = 5:1, and space time = 4 h. On the basis of these results, the maximized process conditions for maximum removal of −COOH peak using the 10 wt % Mo−Al_2O_3 catalyst for the current study were 375 °C, ratio of water-to-OA (v/v) = 5:1, and space time = 4 h, respectively.

The peak for alkenyl =CH stretching at 3004 cm^{-1} (Figures 6 and 7) disappeared for all products obtained using catalyst. This indicates that the 10 wt % Mo−Al_2O_3 catalyst is not only a decarboxylation but also a hydrogenation catalyst (C=C to C−C). There are some other peaks such as C−O stretching and O−H deformation (combined) at 1412 cm^{-1} and out-of-plane O−H bending at 934 cm^{-1}, which also significantly decreased in the liquid product. This corroborates that the Mo−Al_2O_3 catalyst enhances the decarboxylation of OA.

Gas chromatography−Flame Ionization Detection Analysis of Liquid Products. Use of liquid products as commercial fuel largely depends on an understanding of controlling the molecular fingerprint. Figure 8 displays the hydrocarbons identified in the liquid decarboxylated products at the studied experimental conditions using 5 g of 10 wt % Mo−Al_2O_3 catalyst. Selectivity of hydrocarbon varies with temperature, as presented in Figure 8a. The selectivity of tetradecane increased from 0 to 34.8% and pentadecane selectivity decreased from 49.3 to 24% with increasing temperature from 325 to 375 °C. At the same time, the selectivity of hexadecane decreased from 39 to 22.9% and the selectivity of hetadecane slightly increased from 10.7 to 18.3%. Lower heptadecane and higher tetradecane selectivities at 375 °C indicate that the Mo-based catalyst cracks OA into smaller hydrocarbons.

Selectivities of hydrocarbon compounds vary with the space time and water-to-OA (v/v) ratio. Figure 8b,c shows the effect of water-to-OA ratio and space time on the distribution of hydrocarbon compounds in the liquid decarboxylated products. The selectivity of tetradecane increased (from 34.8 to 77%) with decreasing water-to-OA ratio (v/v) from 5:1 to 2:1 and decreased (from 34.8 to 14.5) with decreasing space time from 4 to 0.5 h. The selectivity of pentadecane increased (from 7.2 to 24% and 9.2 to 24%) with increasing ratio (v/v) from 2:1 to 5:1 and space time from 0.5 to 4 h, respectively. The selectivity of hexadecane slightly increased with increasing ratio (v/v) of water-to-OA and space time. The selectivity of heptadecane increased with increasing ratio and decreased with increasing space time. The results conclude that higher temperature and lower water-to-OA ratio (v/v) and space time favor higher selectivity of hepatadecane (73.6%), whereas higher temperature, water-to-OA ratio (v/v), and space time provide higher tetradecane selectivity (34.8%). Lower selectivity of heptadecene for all catalytic experiments indicates a higher degree of saturation of C=C to C−C. This result is consistent with the ATR−FTIR results.

Mass balances for all experiments in this study were found to be in the range of 97 to 99%. Figure S5 shows the mass balance of the experiment conducted at the maximized reaction conditions. Comparing the conversion and liquid yield or selectivity of the current study and the literature data (Table 4)

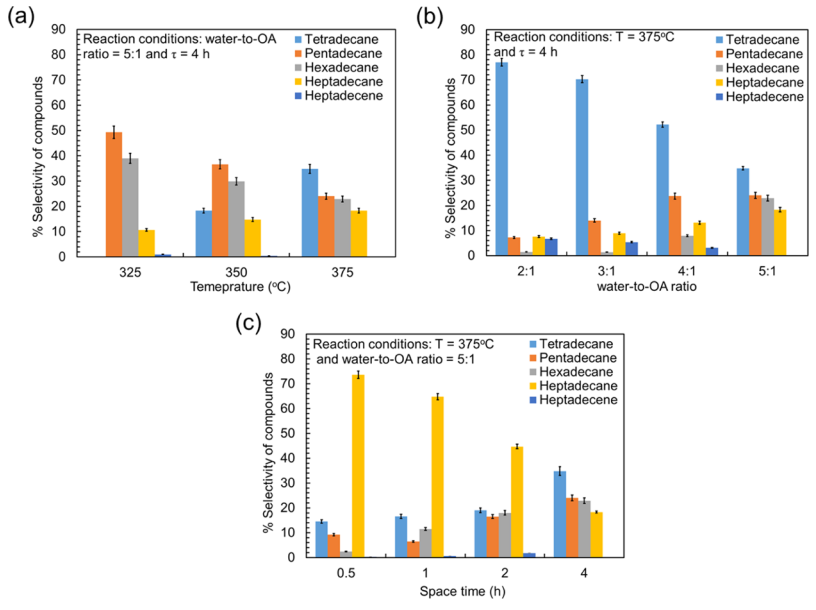

Figure 8. Hydrocarbons present in the liquid products at different (a) temperatures, (b) water-to-OA ratios (v/v), and (c) space times.

DOI: 10.1021/acsomega.8b00562
ACS Omega 2018, 3, 7046−7060

Table 4. Comparison of Conversion and Liquid Yield between the Literature Data and the Current Study[a]

catalyst	feedstock	mode of operation	operating conditions	conversion (%)	overall liquid yield (%)	specific product yield or selectivity (%)
$NiMoS_2/\gamma$-Al_2O_3[62]	refined palm kernel oil	continuous	330 °C, H_2 atmosphere, 1 h^{-1} of LHSV	100	∼92	58 (selectivity of C10−C12)
$NiMoS_2/\gamma$-Al_2O_3[62]	refined palm oil	continuous	330 °C, H_2 atmosphere, 1 h^{-1} of LHSV	100	∼98	58 (selectivity of C10−C12)
$NiMo/\gamma$-Al_2O_3 and $NiMoS_2/\gamma$-Al_2O_3[63]	crude palm oil	continuous	350 °C, H_2 atmosphere, 2 h^{-1} of LHSV (pilot scale)	100	∼100	n/a
$NiMoS_2/\gamma$-Al_2O_3[64]	refined palm kernel oil	continuous	330 °C, H_2 atmosphere, 1 h^{-1} of LHSV	100	∼89	>95.5 (*n*-alkane yield)
$NiMoS_2/\gamma$-Al_2O_3[37]	food grade rapeseed oil	continuous	280 °C, H_2 atmosphere, 0.25−4 h of contact time (V/F)	80−100	>90	n/a
commercial $NiMo/\gamma$-Al_2O_3 and conventional in situ sulfidation by DDS[65]	waste cooking oil (mainly sunflower oil)	continuous	350−390 °C, H_2 atmosphere, 0.5−2 h^{-1} of LHSV	>95	73−82	96.8−97.9 (diesel selectivity)
Pd/mesoporous C[21]	tall oil fatty acid	batch	350 °C, H_2 atmosphere, 5.5 h of reaction time	59	n/a	91 (selectivity of heptadecane and heptadecene)
Pd/SiO_2[66]	lauric acid	batch	300 °C, H_2 atmosphere, 4 h of reaction time	100	n/a	96 (*n*-undecane yield)
Pd/Al_2O_3[66]	lauric acid	batch	300 °C, H_2 atmosphere, 4 h of reaction time	100	n/a	94 (*n*-undecane yield)
Pd/C[67]	lauric acid	batch	300 °C, H_2 atmosphere, 5 h of reaction time	65	58.4	91 (*n*-undecane selectivity)
Pt/ZIF-67/zeolite 5A[18]	lauric acid	batch	320 °C, 2 h of reaction time, CO_2 atmosphere	95	n/a	93.5 (*n*-undecane selectivity)
Ni/HZSM[68]	methyl laurate	batch	280 °C, H_2 atmosphere, 5 h of reaction time	69−86	n/a	27−68 (yield of C11 to C12)
Pt/ZIF-67/zeolite 5A[18]	palmitic acid	batch	320 °C, 2 h of reaction time, CO_2 atmosphere	95	n/a	91.7 (pentadecane selectivity)
Ni/ZrO_2[34]	palmitic acid	batch	300 °C, H_2 atmosphere in the presence of H_2O, 6 h of reaction time	88.2	66.8	30.2 (pentadecane yield)
Ni/ZrO_2[34]	palmitic acid	batch	300 °C, H_2 atmosphere, 6 h of reaction time	88	61	30.2 (pentadecane yield)
Pd/CNT[69]	palmitic acid	batch	260 °C, H_2 atmosphere, 4 h of reaction time	93.3	n/a	85.4 (pentadecane selectivity)
MoO_2/CNT[69]	palmitic acid	batch	260 °C, H_2 atmosphere, 4 h of reaction time	100	n/a	15.4 (pentadecane selectivity)
Pt/C[8]	palmitic acid	batch	290 °C, hydrothermal conditions, 6 h of reaction time	90	90	98 (pentadecane selectivity)
Pd/C[8]	palmitic acid	batch	370 °C, hydrothermal conditions, 3 h of reaction time	n/a	n/a	63 ± 5 (pentadecane yield)
AC[7]	palmitic acid	batch	370 °C, hydrothermal conditions, 3 h of reaction time	33 ± 13	n/a	58 ± 4 (pentadecane selectivity)
NiMCF(9.2T-3D) (R)[70]	palmitic acid	batch	300 °C and 6 h of reaction time	86.4	n/a	31.8 (pentadecane yield)
AC[7]	OA	batch	370 °C, hydrothermal conditions, 3 h of reaction time	80 ± 4	n/a	7 ± 1 (heptadecane selectivity)
Pt/zeollite 5A[19]	OA	batch	320 °C, 2 h of reaction time, H_2 atmosphere	98.7	∼100	72.6 ± 2 (heptadecane selectivity)
Pt/ZIF-67/zeollite 5A[19]	OA	batch	320 °C, 2 h of reaction time, H_2 atmosphere	98.7	∼100	81.5 ± 3 (heptadecane selectivity)
Pt/ZIF-67/zeollite 5A[20]	OA	batch	320 °C, 2 h of reaction time, CO_2 atmosphere	100	∼100	90.5 ± 1.3 (heptadecane yield)
Pt-Ga-MOF[71]	OA	batch	320 °C, 2 h of reaction time, H_2 atmosphere	92	∼84	21.5 (heptadecane selectivity)
Ga-MOF[71]	OA	batch	320 °C, 2 h of reaction time, H_2 atmosphere	66	∼72.4	5.7 (heptadecane selectivity)
Pt/SAPO[72]	OA	batch	325 °C, 2 h of reaction time, H_2 atmosphere	98	n/a	32 (heptadecane yield)
Pt-SAPO-34[73]	OA	batch	325 °C, 2 h of reaction time, H_2 atmosphere	98	91	30 (heptadecane selectivity)
Mo/γ-Al_2O_3 (this study)	OA	continuous	375 °C, hydrothermal conditions, 4 h of space time	91	71	18.3 (heptadecane selectivity)

[a]n/a: data is not available in the cited references.

shows that the decarboxylation study using different reaction conditions such as mode of operation, operating conditions, and catalyst provides various results. Most of the studies reported in the literature have been conducted under an H_2 atmosphere to enhance the decarboxylation reaction. The maximum conversion (∼100%) was obtained using $NiMoS_2/\gamma$-

DOI: 10.1021/acsomega.8b00562
ACS Omega 2018, 3, 7046−7060

Al_2O_3, Ni/ZrO_2, and Pd/SiO_2 catalysts using hydrogen, whereas the current study showed 91% conversion without adding any hydrogen. Table S3 shows the selectivity of heptadecane between the current study and the literature data, which was obtained from OA conversion using different catalysts. The highest heptadecane selectivity reported is 89.3% from OA using activated carbon as the catalyst.[24] The objective of the current study was to find a cost effective metal-supported catalyst for decarboxylation of fatty acids and their derivatives with no added H_2. Our study provided up to 91% conversion of OA (degree of decarboxylation) with a 71% liquid yield at the maximized reaction conditions using the Mo/Al_2O_3 catalyst.

Comparison between the current study and the literature data in terms of selectivity of heptadecane from the catalytic conversion of OA (see Table S3) indicates that the selectivity of heptadecane varies with the process parameters and types of catalysts used. Our study showed 73.6% selectivity for heptadecane using a water-to-oil ratio of 5:1 (v/v) and 0.5 h of space time at 375 °C, with a degree of decarboxylation of 58.6%. On the other hand, the selectivity of heptadecane was 18.3% at 4 h of space time with a degree of decarboxylation of 91%. The results indicate that the Mo catalyst is cracking higher-length hydrocarbon chains at longer space times, increasing the degree of decarboxylation. Although the liquid product in this study contains a broad distribution of hydrocarbons, the liquid product falls within the range of commercial fuels such as kerosene, diesel, and jet fuels (discussed in the following section).

Fuel Quality. Density is an important physical characteristic of liquid fuel, which determines whether it can be used as diesel, kerosene, or jet fuel. For liquids, temperature is an important factor that can affect the density of a liquid with density being expressed at a given temperature for comparison purposes. The values of density at different temperatures of the product obtained at maximized conditions are compared with commercial fuels and listed in Table 5. Comparing the experimental data with conventional fuels indicates that the decarboxylated product falls within the typical diesel range.

Table 5. Density of the Decarboxylated Product and Some Commercial Fuels

compounds	temperature (°C)	density (kg/m^3)
decarboxylated product[a]	15.6	0.85
	21.6	0.85
	25	0.85
	40	0.84
kerosene[74]	15.6	0.78−0.82
jet fuel[75]	15	0.78−0.84
diesel[74]	15.6	0.80−0.96

[a]Maximized conditions.

High heating value (HHV) is the most important parameter for any fuel, which determines the tendency to produce more energy in the engine. Fuels with lower HHV tend to burn inadequately, initiating air pollution.[76] Table 6 shows the HHVs of the obtained decarboxylated products with some commercial fuels. The results indicate that the HHV of the decarboxylated product is similar to jet fuel, kerosene, and diesel.

GC-TCD Analysis of Gaseous Products. Decarboxylation of OA was confirmed by analyzing the gaseous products using GC-TCD. The results obtained at different reaction temperatures are presented in Figure S6. The number of moles of CO and CO_2 were decreased and increased, respectively, with increasing reaction temperature from 325 to 375 °C. This result shows that decarboxylation is the dominating reaction at 375 °C, although 10 wt % $Mo-Al_2O_3$ catalyst slightly cracks the reactant molecules into smaller hydrocarbons. The GC-TCD results help confirm the ATR−FTIR results. Lighter fraction of hydrocarbons was found in the gaseous products, accounting for about 1.75 wt % of the total products (Figure S5).

Table 6. HHVs of Feed, Product, and Commercial Fuels

compounds	HHVs (MJ/kg)
OA	39.2
decarboxylated product[a]	44.7
jet fuel[77]	43.5
kerosene[74]	46.2
diesel[74]	44.8

[a]Maximized conditions.

Decarboxylation of Fatty Acid Derivatives. Hydrothermal decarboxylation of three nonedible feedstocks including castor oil, palm oil, and frying oil (compositions will be found in Tables S4−S6) was performed at the maximized conditions achieved for OA decarboxylation. The maximized conditions are: T = 375 °C, water-to-oil ratio = 5:1(v/v), space time = 4 h, and amount of catalyst = 5 g (10 wt % $Mo-Al_2O_3$). The ATR−FTIR results of the formed products from castor oil, palm oil, and frying oil are shown in Figure 9.

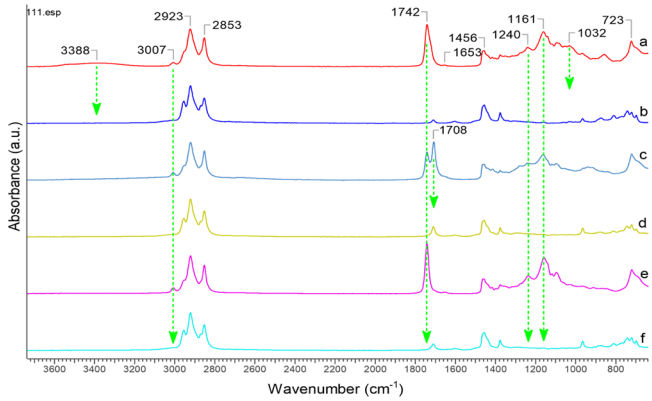

Figure 9. ATR−FTIR spectra of (a) castor oil, (b) the formed product from castor oil, (c) palm oil, (d) the formed product from palm oil, (e) frying oil, and (f) the formed product from frying oil.

In the spectrum of castor oil (Figure 9a), there are several absorbance peaks at 3388, 3007, 2923, 2853, 1742, 1653, 1456, 1240, 1161, 1032, and 723 cm^{-1} resulting from hydroxyl, alkenyl, methylene, and carboxylic ester groups of ricinoleic acid contained in the castor oil. Alcoholic O−H and C−O stretching peaks are observed at 3388 and 1032 cm^{-1}, whereas the peaks at 3007 and 1653 cm^{-1} are ascribed to alkenyl =CH & C=C stretching, respectively. The peaks at 2923, 2853, and 723 cm^{-1} are attributed to methylene C−H asymmetric stretching, symmetric stretching, and rocking modes, respectively. The peak at 1456 cm^{-1} is assigned to methylene C−H scissoring and methyl C−H asymmetric bending modes. The peaks at 1742, 1240, and 1161 cm^{-1} are attributable to

DOI: 10.1021/acsomega.8b00562
ACS Omega 2018, 3, 7046−7060

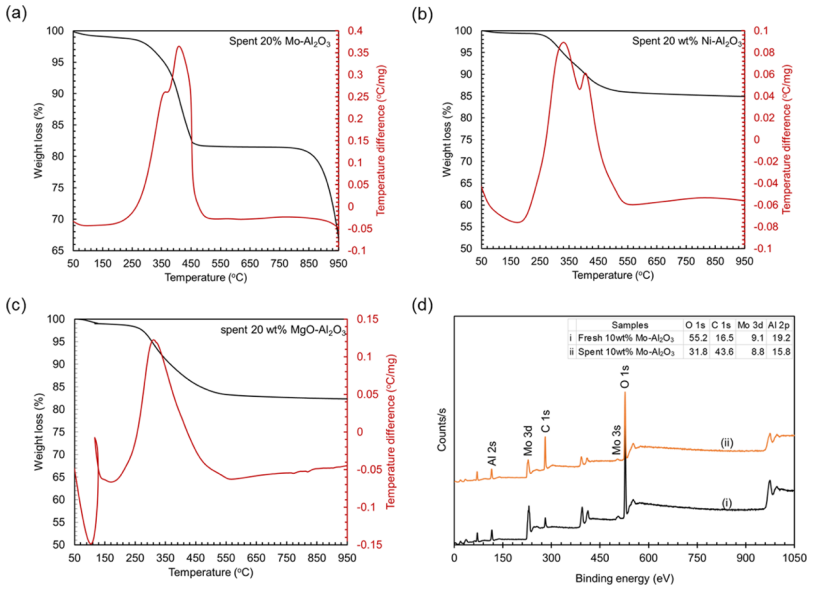

Figure 10. (a–c) TG-DTA of spent catalysts and (d) XPS survey spectra of fresh and spent Mo/Al_2O_3 catalyst.

carboxylic ester C═O stretching and C−O stretching modes of the glycerol ester, respectively. After the decarboxylation reaction, C═O, C−O, O−H, C═C, and ═C−H peaks disappear, whereas a few new peaks appear with the peak at 1711 cm^{-1} being ascribed to the carboxylic C═O stretching mode (Figure 9b). These results confirm the conversion of carboxylic ester (C(═O)−O), alcoholic OH, and alkenyl (C═C) groups and formation of small amount of carboxylic acid (−COOH).

In comparison to the spectrum of castor oil (Figure 9a), the spectrum of palm oil (Figure 9c) shows an additional absorbance peak at 1708 cm^{-1}, which is ascribed to the C═O stretching of the carboxylic acid group contained in palm oil. Similar to that seen for castor oil (Figure 9b), after the decarboxylation reaction, C═O, C−O, C═C, and ═C−H peaks disappear, whereas the peak at 1708 cm^{-1} decreases significantly. These results confirm the conversion of carboxylic ester (C(═O)−O), carboxylic acid (−COOH), and alkenyl (C═C) groups.

The spectrum of frying oil is displayed in Figure 9e. Similar to that of castor oil (Figure 9b), after the decarboxylation reaction, C═O, C−O, C═C, and ═C−H peaks disappear, whereas a few new peaks appear with the peak at 1711 cm^{-1} being ascribed to carboxylic C═O stretching mode (Figure 9f). These results confirm the conversion of carboxylic ester (C(═O)−O), alcoholic OH, and alkenyl (C═C) groups and formation of small amount of carboxylic acid (COOH).

Decarboxylation of castor, palm, and frying oil was further confirmed by GC-TCD analysis of gaseous products formed during the reaction. Figure S7 shows the number of moles of CO or CO_2 present in the gaseous products. The amounts of CO_2 were found to be 0.88, 0.86, and 0.77 mol in the gaseous products formed during the decarboxylation of castor, frying, and palm oil. On the other hand, the quantities of CO were found to be 0.05, 0.13, and 0.23 mol, respectively. Although complete decarboxylation was not achieved for the above three nonedible feedstocks, our hydrothermal decarboxylation process shows significant feedstock feasibility to decarboxylate any fatty acid or its derivatives without adding any external hydrogen source or hydrogen donor solvent. These results are potentially attractive to implement the process for commercial production of liquid hydrocarbons from various feed sources, which can help lower our dependency on fossil fuels.

Catalyst Deactivation Studies. A metal-supported catalyst has a tendency for deactivation when it is exposed to harsh (high temperature or pressure) hydrothermal environments. Deactivation of a metal catalyst can occur from several factors including adsorption of impurities from the feed/product streams, coke deposition on the catalyst surface, oxidation of metal, metallic surface area reduction from sintering/leaching, and a drop in surface area from pore blockage.[78] XRD analysis was performed on all three spent catalysts (Figure 2). Metal-supported spent catalysts usually show the peaks for graphitic coke formation at $2\theta = 62°$ and atomic coke formation at $2\theta = 30°$, respectively.[5,58] From the XRD pattern, no such peak was found for all three catalysts (Figure 2c,e,g). There were no significant differences observed in the XRD patterns for fresh and spent 10 wt % MgO/Al_2O_3 and 10 wt % Ni/Al_2O_3 catalysts. On the other hand, peak intensities for the spent 10 wt % Mo/Al_2O_3 catalyst were found to be larger than those of its fresh one, indicating catalyst agglomeration from the decarboxylation reaction. Agglomeration of Mo particles may be the main reason for the observed reduction of the BET surface area of spent Mo catalyst compared to the spent MgO and Ni catalysts (Table 2 and Figure S2i). The lower BET surface area observed for the spent Mo catalyst may be due to pore blockage by produced hydrocarbon molecules which did not wash out with hexanes or catalyst drying step. Although all spent catalysts have lower BET surface areas than their fresh ones, they still maintain the mesoporous pore size distributions (Figure S2ii).

The surface morphology of the synthesized catalysts were examined by SEM imaging both before and after the decarboxylation reaction (Figure S8). All fresh catalysts showed uniform metal/metal oxide particle distribution on the surface of the catalysts, indicating better catalytic properties. Although the Ni catalyst has a morphology similar to that of the Mo and MgO catalyst, the Ni catalyst was found to gasify the feedstock at the chosen reaction conditions instead of decarboxylation (explained earlier). The agglom-

DOI: 10.1021/acsomega.8b00562
ACS Omega 2018, 3, 7046−7060

erated structure of the spent 10 wt % Mo−Al_2O_3 catalyst was confirmed from the SEM images. There were no morphological differences observed for the fresh and spent 10 wt % MgO−Al_2O_3 and 10 wt % Ni−Al_2O_3 catalysts. These results are consistent with the XRD and BET results.

Elemental analysis was performed for all three spent catalysts to see the composition differences between their fresh and spent states (Figure S9). The weight percentages of Mo and Ni were found to be 9.58 and 9.23 in the spent catalysts. Slightly lower percentage of Mo and Ni in the spent catalyst does not indicate metal leaching during the decarboxylation reaction. Deposition of impurities (Figure S10) on the catalyst surface may dilute the concentration of Mo and Ni. As mentioned earlier, C found on the fresh catalysts originates from the sample holder. However, the peak intensities of C in all three spent catalysts are significantly larger those of the fresh ones, indicating that the catalysts have carbon deposition from the decarboxylation reaction. Because XRD did not detect any crystalline carbon (atomic or coke), the carbon identified by EDXS analysis is likely amorphous carbon. Amorphous carbon can be simply removed by calcining the catalyst above the reaction temperature under an inert atmosphere.

Thermogravimetry/differential thermal analysis (TG-DTA) was conducted to quantify the deposited carbon on the catalyst surfaces based on the weight loss with increasing temperature (Figure 10a−c). The weight loss and the corresponding DTA peaks in TG-DTA spectra represent burning of three types of carbon such as atomic carbon, amorphous carbon, and graphitic carbon. These three carbons show DTA peaks at three temperature regions such as <250, 250−600, and >600 °C, respectively.[79] No peak was observed for all spent catalysts at >600 °C, which confirms the absence of graphitic coke on the spent catalyst surfaces. The weight losses for spent Mo−Al_2O_3, Ni−Al_2O_3, and MgO−Al_2O_3 are 30, 15, and 18, respectively. These weight losses during TG-DTA correspond to only the formation of atomic and amorphous carbon. Higher amount of carbon deposition on spent Mo−Al_2O_3 catalyst is due to the higher acidity of Mo−Al_2O_3 compared to Ni−Al_2O_3 and MgO−Al_2O_3 catalysts. Higher acidity of catalyst is favorable for higher degree of carbon deposition.[80,81]

XPS survey spectra of fresh and spent 10 wt % Mo−Al_2O_3 catalyst were obtained to provide insight into the Mo catalyst deactivation process (Figure 10d). Carbon in the fresh 10 wt % Mo−Al_2O_3 catalyst corresponds to adventitious carbon which is typically detected in samples that have been exposed to the atmosphere or generated during the analysis. The relative content of C in the fresh catalyst is 16.5%, whereas the amount in the spent catalyst was 43.6%. The difference between the quantities of carbon in fresh and spent catalysts is 27.1%, which is closer to the amount quantified by TG-DTA. Thus, large increase in C on the spent catalyst indicates the deposition from the decarboxylation reaction. This C potentially may be bound with multiple Mo ions, which is hard to remove by simple hexane washing or vacuum drying.[82] The existence of different states of Mo was also confirmed in the spent 10 wt % Mo−Al_2O_3 catalyst using high-resolution XPS spectra (Figure 3b and Table S7). A higher percentage of Mo(IV) (77%) was found in spent sample compared to the fresh one (40%), whereas the Mo(VI) component was decreased from 51 to 11% and the Mo(V) amount remained relatively constant at 9−12%, respectively. Higher percentage of Mo(VI) state compared to other oxidation states on the fresh catalyst surface may be the active catalytic phase of decarboxylation. The results also indicates that reduction of Mo (VI) to Mo(IV) was occurring by in situ hydrogen during decarboxylation of fatty acids.

Catalyst Stability, Reusability, and Regeneration. Catalyst stability is an important factor for commercializing any catalytic process. Formation of graphitic coke on the metal-supported catalyst surface mainly poisons the active sites of the catalyst and reduces activity during the reaction. Graphitic coke formation also prevents the reusability of any catalyst as it is very hard to burn off the graphitic carbon during regeneration step. Stability study of Mo−Al_2O_3 was conducted at the maximized reaction conditions until the catalyst starts to deactivate. ATR−FTIR spectra of decarboxylated liquid products at the maximized reaction conditions at 132 h (5.5 days) time on stream are shown in Figure 11.

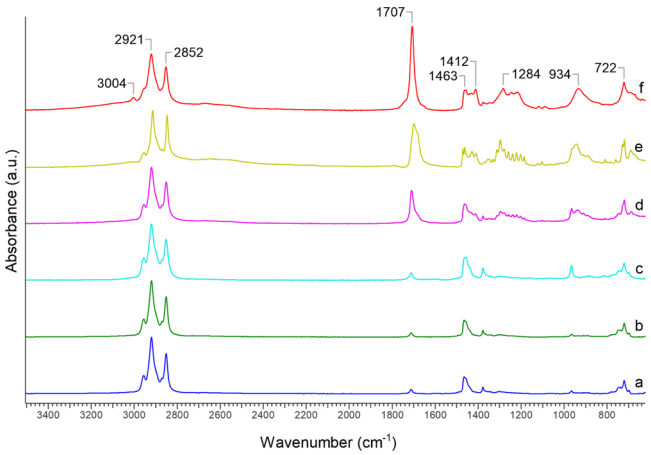

Figure 11. FTIR spectra of (a−e) the decarboxylated products at 132 h time on stream: (a) 24; (b) 48; (c) 72; (d) 96; (e) 132 h; and (f) OA.

Deactivation of the catalyst was measured by the degree of decarboxylation obtained at different time of streams. Figure 11 shows that the degree of decarboxylation (~92%) was consistent over 72 h time on stream. This is the maximum degree of decarboxylation obtained for this study. The degree of decarboxylation started decreasing afterward. The values of degree of decarboxylation obtained after 96 and 132 h time on stream were 60 and 48%, respectively. Decreasing trend of degree of decarboxylation indicates that the catalyst is losing its activity during the reaction. EDXS, XPS, and TG-DTA of spent catalysts showed that a significant amount of carbon (atomic and amorphous) was deposited on the catalyst surface during decarboxylation reaction which is deactivating the catalyst. Deposited carbon is blocking the actives sites of catalysts, which is retarding the decarboxylation of OA. The disappearance of =C−H peak (~3004 cm^{-1}) during 132 h time on stream indicates that the catalyst was active to saturate the final products.

Deactivation of the catalyst necessitates to regeneration step because the degree of decarboxylation obtained using spent catalyst was only 25% (Figure S11). Because only atomic and amorphous carbon deposition were observed, it is easy to remove these types of carbon by burning them off in the presence of air. Spent Mo−Al_2O_3 catalyst (from stability study) was regenerated by simply burning with air followed by reduction afterward and reused second time for decarboxylation of OA at the maximized reaction conditions. ATR−

DOI: 10.1021/acsomega.8b00562
ACS Omega 2018, 3, 7046−7060

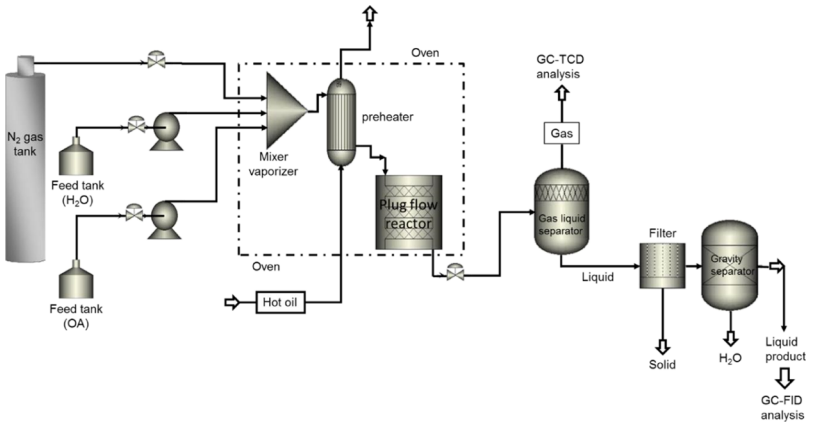

Figure 12. Schematic of continuous reactor setup.

FTIR spectra of decarboxylated liquid products using regenerated Mo−Al_2O_3 catalyst are presented in Figure S11 along with the spectra of fresh and spent catalyst for comparison. The degree of decarboxylation obtained using regenerated Mo−Al_2O_3 catalyst was 70%, whereas the value was 92% using fresh catalyst. The regenerated catalyst was not able to achieve the same degree of decarboxylation which may be due to the agglomeration of metal particles after first use. Agglomeration of Mo particles in the spent catalyst was confirmed by SEM imaging and CO pulse chemisorption experiment (Figure S8 and Table 3) measuring the percent metal dispersion and active particle size. The degree of decarboxylation using regenerated catalyst was 70% during 72 h time on stream and started decreasing afterward.

XRD patterns of regenerated and spent regenerated catalysts have the similar trend except the intensity difference (Figure S12a). The broad peaks of spent regenerated catalyst indicate that the metal particles are agglomerating to make bigger particle size during decarboxylation reaction. The formation of deposited carbon on the surface of spent regenerated catalyst is quantified by TG-DTA, which is about 12 wt % (Figure S12b). The formation of carbon on the catalyst surface during decarboxylation indicates that it is hard to prevent. The BET surface area and pore volume of regenerated catalyst are 102 m^2/g and 0.30 cm^3/g, whereas the values are 70 m^2/g and 0.22 m^3/g, respectively. N_2 adsorption−desorption isotherms of regenerated and spent regenerated Mo−Al_2O_3 catalyst have the similar pattern as fresh and spent catalysts. BJH pore size distributions in both cases slightly shift to large pore diameter range but still maintain the mesoporosity (Figure S12c). The surface morphology of spent regenerated catalyst also indicates the agglomerated structure of the catalyst (Figure S12d).

CONCLUSIONS

This work investigated three different catalysts including 10 wt % Mo−Al_2O_3, 10 wt % MgO−Al_2O_3, and 10 wt % Ni−Al_2O_3 and showed that the Mo catalyst is an efficient catalyst for decarboxylation of OA and their derivatives in subcritical water. The maximized conditions for higher degree of decarboxylation of OA (92%) and liquid yield (71%) were found to be 375 °C, water-to-OA ratio of 5:1 (v/v), and space time of 4 h using 5 g of 10 wt % Mo−Al_2O_3 catalyst. The Mo catalyst was found to crack the OA into smaller hydrocarbon molecules. The selectivities of OA to hydrocarbons obtained at maximized reaction conditions were 34.8% tetradecane, 24% pentadecane, 22.9% hexadecane, and 18.3% heptadecane. The Mo catalyst was also found to hydrogenate C═C to C−C with no added hydrogen. This hydrothermal approach for decarboxylating real feedstocks such as castor oil, palm oil, and frying oil is found to be promising to produce oxygen-free liquid hydrocarbons.

The deactivation studies of catalysts showed that the Mo catalyst was slightly agglomerated compared to Ni and MgO catalysts. No graphitic coke was found in the three evaluated catalysts but higher amount of amorphous coke was detected in the Mo catalyst surface because of its high acidity. Amorphous coke is easy to remove by simple calcination and the catalyst can be reused.

EXPERIMENTAL SECTION

Materials. OA (90%), castor oil, hexanes (ACS Grade), nickel nitrate hexahydrate [$Ni(NO_3)_2{\cdot}6H_2O$], ammonium molybdate tetrahydrate [$(NH4)_6Mo_7O_{24}{\cdot}4H_2O$], and magnesium sulfate heptahydrate [$MgSO_4{\cdot}7H_2O$] were obtained from Sigma-Aldrich, Canada, and are used as received. Alumina (γ-Al_2O_3) powder (Catalox SSCa 5/200) was obtained from SASOL. Frying oil (used canola oil) was obtained from author's home and filtered to remove solid particles before use. Palm oil was obtained from Malaysia. A compact ultrapure water system (EASY pure LF, Mandel Scientific Co., model BDI-D7381) was used to obtain deionized water (18.2 MΩ).

Catalyst Synthesis. Ni, Mo, and MgO supported on γ-Al_2O_3 catalyst were synthesized using an incipient impregnation method.[61,83] γ-Al_2O_3 was chosen as the support because it has larger surface area and pore volume and higher acidity compared to other phases of Al_2O_3 (results will be found in Supporting Information, Figure S13). Larger surface area provides more active sites and a higher acidic catalyst[33] is favorable for decarboxylation. For a standard synthesis, the desired amount of metal precursor for 10 wt % loading was dissolved in deionized water equivalent to 120 vol % of pore volume of alumina (0.50 cm^3/gm). For example, 1 g of 10 wt % Ni−Al_2O_3 catalyst requires 0.50 g of $Ni(NO3)_2{\cdot}6H_2O$ and 0.9 g of Al_2O_3, 1 g of 10 wt % Mo catalyst requires 0.18 g of $(NH_4)_6Mo_7O_{24}{\cdot}4H_2O$ and 0.9 g of Al_2O_3, 1 g of 10 wt % MgO requires 0.64 g of $MgSO_4{\cdot}7H_2O$ and 0.9 g of Al_2O_3, respectively. The required support (alumina) was immersed into the metal solution at once for better dispersion. The wet catalyst was placed into a vacuum oven at 80 °C overnight. The dry powder was then calcined into a muffle furnace at 600 °C @ 5 °C/min for 4 h. Hydrogen reduction with 5 vol % H_2 balanced with N_2 at 950 °C @ 3 °C/min for 2 h was

DOI: 10.1021/acsomega.8b00562
ACS Omega 2018, 3, 7046−7060

performed afterward for Ni and Mo catalysts only. The actual metal loadings were confirmed by EDXS and XPS analysis.

Catalyst Testing. Decarboxylation of OA and its derivatives was performed in a benchtop reaction system (BTRSJR, Autoclave Engineers, Erie, PA) with a maximum allowable working pressure of 2900 psi @ 650 °C. Figure 12 represents the detailed reactor setup. The system has a 10 mL tubular reactor (316 stainless steel reactor tube with type 316 stainless steel fittings) assembled with a furnace. The furnace temperature was set 20 °C higher than the reaction temperature. The reactor is connected with four feed lines for feeding either gas or liquids. All feeds were mixed and vaporized into a mixer vaporizer before feeding to the reactor. The feed stream then passed through the reactor. The mixer is placed into an oven to preheat the feed mixture, whereas the maximum oven temperature is 250 °C. A gas−liquid separator is placed next to the reactor outside the oven. The separator is surrounded by a cooling arrangement connected with a chiller, with the chiller temperature maintained at 6 °C during the reaction to separate the gas and liquid phases.

Before starting any experiment, the reactor was washed thoroughly with soapy water, clean water, and then hexanes to remove any residuals from previous experiments. Air was passed through the reactor to remove any water or hexane sticking to the walls. Catalyst (5 g) was loaded for each experiment into the reactor with quartz wool being placed at the top and bottom of the reactor to maintain the catalyst inside. All fittings were attached to the reactor, which was then placed into the furnace. The main power of the system was turned on and the oven temperature was set to the desired reaction temperature. The reaction temperature was varied from 325 to 400 °C according to the experimental methodology explained below. During the reactor heating, N_2 gas was flowed through the reactor to remove any oxygen. N_2 flow was then stopped and the reactor outlet was opened to remove any N_2 from the system. Two reactants (OA/its derivatives) and water were then fed to the reactor continuously. Each experiment was run for a minimum of 24 h and repeated at least three times in this study and the average results are reported. The space time (τ) was calculated from the volume of the catalyst (amount of catalyst/packed density of catalyst) divided by the reactant flow rate. Both reactants (fatty acid/derivatives and water) were accounted to calculate the flow rates at ambient T and P. The liquid and gaseous products were then collected and analyzed continuously from the gas−liquid separator until the catalyst started to deactivate. The liquid product was stored in glass vials. An air tight Tedler gas bag (SKC Inc., PA) was used to store the gaseous product for analysis. The spent catalyst collected for each run was thoroughly washed with excess hexanes. Hexanes were discarded from the solid catalyst. Liquid products which were stuck into catalyst bed were collected afterward during hexane evaporation. The wet solid catalyst was then dried at 80 °C for 12 h in a vacuum oven. The liquid product yield is calculated as the weight of the liquid product after reaction divided by the amount of OA fed to the reactor, whereas the gaseous product yield is (1—liquid product yield).

Product Analysis. Types of hydrocarbons present in the liquid product was quantified using a Shimadzu, GC-2014 equipped with a flame ionization detector and a capillary DB WAX column (Agilent Technologies, Santa Clara, CA, USA) (dimension: 30 m × 0.250 mm × 0.25 μm, temperature limit: 20 to 260 °C). Helium, hydrogen, and helium-air were used as the carrier, flame, and makeup gas, respectively. The oven temperature programming was followed from Hossain et al.[84] Retention times of known standards such as C8−C20 saturated hydrocarbons and heptadecene (Sigma-Aldrich, Oakville, ON) were used to identify the types of hydrocarbons in the liquid product. Sample (1 μL) with a 10:1 split ratio was injected manually into the column. Repetitive injection for each sample was performed until the similar peak area of interested compounds was obtained. Selectivity of hydrocarbons present in the liquid product was calculated from the following equation[85−87]

$$\text{Selectivity of hydrocarbon} = \frac{\text{peak area of individual hydrocarbon}}{\text{total peak area of all hydrocarbons of interest}} \quad (1)$$

The injector and detector temperatures were retained at 200 and 250 °C, respectively.

Infrared spectra (600−4000 cm^{-1} with a resolution of 4 cm^{-1} over 64 scans) of feed and liquid products were collected using an ATR−FTIR spectroscope (Nicolet 6700 FTIR, Thermo Scientific). Degree of decarboxylation was calculated using the following equation

$$\text{Degree of decarboxylation} = \frac{[-\text{COOH peak area}]_{\text{OA\_initial}} - [-\text{COOH peak area}]_{\text{product}}}{[-\text{COOH peak area}]_{\text{OA\_initial}}} \times 100 \quad (2)$$

An Eagle Eye SG-Ultra Max Hydrometer (Density meter) [dimension = 5.5″ W × 5.5″ D × 1″ H (outside)] and IKA C2000 bomb calorimeter were used to measure density and HHVs of the liquid products.

Gaseous products formed during decarboxylation reaction were measured using a mixture of standard calibration gases (H_2, N_2, O_2, CH_4, CO, and CO_2). Gas sample (1 mL) using an SGE gas tight syringe (model number 008100, Reno, NV USA) was injected manually into a nickel packed column (120/80 Hayesep D stainless steel 3.18 mm ID, 6.2 m L) of Shimadzu, GC-2014 (He as the carrier gas) which is connected with a thermal conductivity detector. The oven temperature was held at 35 °C for 6 min followed by 25 °C/min ramp and 1 min hold at 200 °C. The injector and detector temperatures were maintained at 200 and 250 °C, respectively. Injection was repeated multiple times for accuracy. Lighter fractions of hydrocarbons (C2 to C4) were quantified as the total no of moles of gas produced minus the number of moles of known gas.

Catalyst Characterization. *N_2-Physisorption.* A Tristar II 3020 (Micromeritics Instrument Corporation, Norcross, GA, USA) instrument was used to determine the BET surface area and BJH pore size distributions of the fresh and spent catalysts at −193 °C using 99.995% pure N_2 gas obtained from Praxair (Oakville, Canada). Approximately, 80 mg of each catalyst sample was degassed under an N_2 atmosphere at 150 °C overnight before measurements. Degassing enhances the removal of the adsorbed moisture from the catalyst surface.

XRD Analysis. Crystallinity of catalyst samples was analyzed using a Bruker D2 Phaser powder diffractometer over 2θ = 10−80° using a scan rate of 0.1°/min and Cu Kα radiation (λ for Kα is equal to 1.54059 Å).

H_2-TPR Analysis. An Autochem II 2920 analyzer (Micromeritics Instrument Corporation, Norcross, GA, USA) equipped with a thermal conductivity detector was used to

DOI: 10.1021/acsomega.8b00562
ACS Omega 2018, 3, 7046−7060

obtain the TPR profiles of fresh catalysts by flowing 10% H_2 balanced Ar at a rate of 50 mL/min. A minimum of 140−150 mg of the catalyst sample was used for each analysis. The temperature was increased from room temperature to 1100 °C @ 10 °C/min.

CO Pulse Chemisorption. An Autochem II 2920 analyzer was used to determine the active particle diameter, the % metal dispersion, and the active metal surface area of catalyst samples using a series of 1 mL of CO pulses (10% CO balanced with Ar) injected into the catalyst sample at 40 °C. The catalyst sample was pretreated with a stream of Ar (50 mL/min) before CO pulses were injected.

NH_3-TPD Analysis. NH_3 TPD analysis was conducted using a Micromeritics Autochem II 2920 analyzer coupled with a thermal conductivity detector. Samples were pretreated at 400 °C @ 15 °C/min for 1 h under helium. The sample was then cooled from 400 to 100 °C using 10% NH_3 balanced with He (50 cm^3/min) for another hour. NH_3 flow was then stopped and He (50 cm^3/min) was flowed at 100 °C for 1 h to remove any physically adsorbed NH_3. The temperature was then increased to 850 °C @ 15°/min for desorption of NH_3 from the catalyst surface. The holding time at 850 °C was 1 h. The acidity of the catalysts was calculated from the amount of NH_3 desorbed from the acid sites of the catalyst during the desorption process which was monitored by the thermal conductivity detector.

TEM and SEM Imaging. The morphologies of both the fresh and spent catalysts were obtained from TEM (model JEOL 2010F) and SEM imaging (LEO 1530).

EDXS Analysis. Elemental composition of fresh and spent catalysts was confirmed and quantified by using the EDXS feature of the scanning electron microscope.

XPS Analysis. XPS analysis of fresh and spent catalyst samples was conducted with a Kratos Axis Ultra spectrometer using a monochromatic Al Kα source (15 mA, 14 kV).

■ ASSOCIATED CONTENT

Supporting Information

The Supporting Information is available free of charge on the ACS Publications website at DOI: 10.1021/acsomega.8b00562.

EDXS analysis of fresh catalysts; N_2 adsorption−desorption isotherms and pore size distributions of fresh and spent catalysts; GC-TCD analysis of product gases using different catalysts such as 10 wt % MgO−Al_2O_3, 10 wt % Ni−Al_2O_3, and 10 wt % Mo−Al_2O_3; percentage removal of −COOH group at different temperatures, water-to-OA ratios, and space times; mass balance at the maximized reaction conditions; number of moles of CO and CO_2 present in the gas product; identification of CO and CO_2 in the gaseous products formed during decarboxylation of castor, palm, and frying oil; SEM images of fresh and spent catalysts: (a,b) 10 wt % Mo/Al_2O_3; (c,d) 10 wt % MgO/Al_2O_3; and (e,f) 10 wt % Ni/Al_2O_3; EDXS analysis of spent catalysts; ATR−FTIR spectra of (a) fresh, (b) spent, and (c) regenerated Mo/Al_2O_3 catalysts; FTIR spectra of the decarboxylated products using (a) fresh, (b) regenerated, (c) spent Mo/Al_2O_3 catalysts, and (d) OA; characterization of regenerated and spent regenerated Mo/Al_2O_3 catalyst: (a) XRD patterns of regenerated and spent regenerated samples; (b) TG-DTA profiles of spent regenerated sample; (c) N_2 adsorption−desorption isotherms and BJH pore size distributions of regenerated and spent regenerated samples; and (d) SEM image of spent regenerated sample; NH_3-TPD profiles and pore properties of γ- and θ-Al_2O_3 (θ-Al_2O_3 was obtained by calcining γ-Al_2O_3 at 1100 °C for 1 h @ 10 °C); XPS chemical shifts of fresh Mo−Al_2O_3 catalyst; carbon balance using 10 wt % MgO/Al_2O_3, 10 wt % Ni/Al_2O_3, and 10 wt % Mo/Al_2O_3 catalysts at 375 °C, space time of 4 h, and water-to-OA (v/v) ratio of 5:1 using 5 g of catalyst; comparison of heptadecane selectivity reported in the literature and the current study, which was obtained from catalytic conversion of OA; compositions of castor oil, palm oil, and canola oil; and XPS chemical shifts of spent Mo/Al_2O_3 catalyst (PDF)

■ AUTHOR INFORMATION

Corresponding Author

*E-mail: pcahrpentier@eng.uwo.ca. Phone: 1 (519) 661-3466. Fax: 1 (519) 661-3498 (P.A.C.).

ORCID

Md Zakir Hossain: 0000-0003-0310-6321

William Z. Xu: 0000-0002-3460-8474

Notes

The authors declare no competing financial interest.

■ ACKNOWLEDGMENTS

This project was funded by BioFuelNet Canada, the Ontario Centre of Excellence (OCE-TalentEdge) program, the Natural Science and Engineering Research Council (NSERC), and Greenfield global and Audro Energy. We would like to acknowledge Dr Tim Goldhawk, Western Nanofabrication Facility for SEM and EDX analysis and Dr Pastor Solano-Flores, Research Technician, Dept. of Chemical and Biochemical Engg., Western University for helping with the reactor troubleshooting.

■ REFERENCES

(1) Demirbaş, A. Biodiesel fuels from vegetable oils via catalytic and non-catalytic supercritical alcohol transesterifications and other methods: a survey. *Energy Convers. Manage.* **2003**, *44*, 2093−2109.

(2) Ramos, M. J.; Fernández, C. M.; Casas, A.; Rodríguez, L.; Pérez, Á. Influence of fatty acid composition of raw materials on biodiesel properties. *Bioresour. Technol.* **2009**, *100*, 261−268.

(3) Sivasamy, A.; Cheah, K. Y.; Fornasiero, P.; Kemausuor, F.; Zinoviev, S.; Miertus, S. Catalytic applications in the production of biodiesel from vegetable oils. *ChemSusChem* **2009**, *2*, 278−300.

(4) Snåre, M.; Kubičková, I.; Mäki-Arvela, P.; Eränen, K.; Murzin, D. Y. Heterogeneous catalytic deoxygenation of stearic acid for production of biodiesel. *Ind. Eng. Chem. Res.* **2006**, *45*, 5708−5715.

(5) Hossain, M. Z.; Jhawar, A. K.; Chowdhury, M. B. I.; Xu, W. Z.; Wu, W.; Hiscott, D. V.; Charpentier, P. A. Using Subcritical Water for Decarboxylation of Oleic Acid into Fuel-Range Hydrocarbons. *Energy Fuels* **2017**, *31*, 4013−4023.

(6) Fu, J.; Lu, X.; Savage, P. E. Hydrothermal decarboxylation and hydrogenation of fatty acids over Pt/C. *ChemSusChem* **2011**, *4*, 481−486.

(7) Fu, J.; Shi, F.; Thompson, L. T., Jr.; Lu, X.; Savage, P. E. Activated carbons for hydrothermal decarboxylation of fatty acids. *ACS Catal.* **2011**, *1*, 227−231.

(8) Fu, J.; Lu, X.; Savage, P. E. Catalytic hydrothermal deoxygenation of palmitic acid. *Energy Environ. Sci.* **2010**, *3*, 311−317.

DOI: 10.1021/acsomega.8b00562
ACS Omega 2018, 3, 7046−7060

(9) Hollak, S. A. W.; Gosselink, R. W.; van Es, D. S.; Bitter, J. H. Comparison of tungsten and molybdenum carbide catalysts for the hydrodeoxygenation of oleic acid. *ACS Catal.* **2013**, *3*, 2837−2844.
(10) Snåre, M.; Mäki-Arvela, P.; Simakova, I. L.; Myllyoja, J.; Murzin, D. Y. Overview of catalytic methods for production of next generation biodiesel from natural oils and fats. *Russ. J. Phys. Chem. B* **2009**, *3*, 1035−1043.
(11) Yeh, T. M.; Dickinson, J. G.; Franck, A.; Linic, S.; Thompson, L. T.; Savage, P. E. Hydrothermal catalytic production of fuels and chemicals from aquatic biomass. *J. Chem. Technol. Biotechnol.* **2013**, *88*, 13−24.
(12) Peterson, A. A.; Vogel, F.; Lachance, R. P.; Fröling, M.; Antal, M. J., Jr.; Tester, J. W. Thermochemical biofuel production in hydrothermal media: A review of sub- and supercritical water technologies. *Energy Environ. Sci.* **2008**, *1*, 32−65.
(13) Jayasinghe, P.; Hawboldt, K. A review of bio-oils from waste biomass: Focus on fish processing waste. *Renewable Sustainable Energy Rev.* **2012**, *16*, 798−821.
(14) Siddiquee, M. N.; Rohani, S. Lipid extraction and biodiesel production from municipal sewage sludges: a review. *Renewable Sustainable Energy Rev.* **2011**, *15*, 1067−1072.
(15) Brennan, L.; Owende, P. Biofuels from microalgae-A review of technologies for production, processing, and extractions of biofuels and co-products. *Renewable Sustainable Energy Rev.* **2010**, *14*, 557−577.
(16) Yeh, T. M.; Hockstad, R. L.; Linic, S.; Savage, P. E. Hydrothermal decarboxylation of unsaturated fatty acids over PtSnx/C catalysts. *Fuel* **2015**, *156*, 219−224.
(17) Sotelo-Boyás, R.; Liu, Y.; Minowa, T. Renewable diesel production from the hydrotreating of rapeseed oil with Pt/Zeolite and $NiMo/Al_2O_3$ catalysts. *Ind. Eng. Chem. Res.* **2011**, *50*, 2791−2799.
(18) Yang, L.; Carreon, M. A. Deoxygenation of palmitic and lauric acids over Pt/ZIF-67 membrane/zeolite 5A bead catalysts. *ACS Appl. Mater. Interfaces* **2017**, *9*, 31993−32000.
(19) Yang, L.; Tate, K. L.; Jasinski, J. B.; Carreon, M. A. Decarboxylation of oleic acid to heptadecane over Pt supported on zeolite 5A beads. *ACS Catal.* **2015**, *5*, 6497−6502.
(20) Yang, L.; Carreon, M. A. Effect of reaction parameters on the decarboxylation of oleic acid over Pt/ZIF-67membrane/zeolite 5A bead catalysts. *J. Chem. Technol. Biotechnol.* **2017**, *92*, 52−58.
(21) Mäki-Arvela, P.; Rozmysłowicz, B.; Lestari, S.; Simakova, O.; Eränen, K.; Salmi, T.; Murzin, D. Y. Catalytic deoxygenation of tall oil fatty acid over palladium supported on mesoporous carbon. *Energy Fuels* **2011**, *25*, 2815−2825.
(22) Dragu, A.; Kinayyigit, S.; García-Suárez, E. J.; Florea, M.; Stepan, E.; Velea, S.; Tanase, L.; Collière, V.; Philippot, K.; Granger, P.; Parvulescu, V. I. Deoxygenation of oleic acid: Influence of the synthesis route of Pd/mesoporous carbon nanocatalysts onto their activity and selectivity. *Appl. Catal., A* **2015**, *504*, 81−91.
(23) Simakova, I.; Rozmysłowicz, B.; Simakova, O.; Mäki-Arvela, P.; Simakov, A.; Murzin, D. Y. Catalytic deoxygenation of C18 fatty acids over mesoporous Pd/C catalyst for synthesis of biofuels. *Top. Catal.* **2011**, *54*, 460−466.
(24) Hossain, M. Z.; Chowdhury, M. B. I.; Jhawar, A. K.; Xu, W. Z.; Charpentier, P. A. Continuous low pressure decarboxylation of fatty acids to fuel-range hydrocarbons with in situ hydrogen production. *Fuel* **2018**, *212*, 470−478.
(25) Boda, L.; Onyestyák, G.; Solt, H.; Lónyi, F.; Valyon, J.; Thernesz, A. Catalytic hydroconversion of tricaprylin and caprylic acid as model reaction for biofuel production from triglycerides. *Appl. Catal., A* **2010**, *374*, 158−169.
(26) Tiwari, R.; Rana, B. S.; Kumar, R.; Verma, D.; Kumar, R.; Joshi, R. K.; Garg, M. O.; Sinha, A. K. Hydrotreating and hydrocracking catalysts for processing of waste soya-oil and refinery-oil mixtures. *Catal. Commun.* **2011**, *12*, 559−562.
(27) Peng, B.; Yuan, X.; Zhao, C.; Lercher, J. A. Stabilizing catalytic pathways via redundancy: selective reduction of microalgae oil to alkanes. *J. Am. Chem. Soc.* **2012**, *134*, 9400−9405.
(28) Peng, B.; Yao, Y.; Zhao, C.; Lercher, J. A. Towards quantitative conversion of microalgae oil to diesel-range alkanes with bifunctional catalysts. *Angew. Chem.* **2012**, *124*, 2114−2117.
(29) Morgan, T.; Santillan-Jimenez, E.; Harman-Ware, A. E.; Ji, Y.; Grubb, D.; Crocker, M. Catalytic deoxygenation of triglycerides to hydrocarbons over supported nickel catalysts. *Chem. Eng. J.* **2012**, *189*, 346−355.
(30) Wu, J.; Shi, J.; Fu, J.; Leidl, J. A.; Hou, Z.; Lu, X. Catalytic Decarboxylation of Fatty Acids to Aviation Fuels over Nickel Supported on Activated Carbon. *Sci. Rep.* **2016**, *6*, 27820.
(31) Na, J.-G.; Yi, B. E.; Kim, J. N.; Yi, K. B.; Park, S.-Y.; Park, J.-H.; Kim, J.-N.; Ko, C. H. Hydrocarbon production from decarboxylation of fatty acid without hydrogen. *Catal. Today* **2010**, *156*, 44−48.
(32) Zhao, X.; Wei, L.; Cheng, S.; Kadis, E.; Cao, Y.; Boakye, E.; Gu, Z.; Julson, J. Hydroprocessing of carinata oil for hydrocarbon biofuel over $Mo-Zn/Al_2O_3$. *Appl. Catal., B* **2016**, *196*, 41−49.
(33) Hengst, K.; Arend, M.; Pfützenreuter, R.; Hoelderich, W. F. Deoxygenation and cracking of free fatty acids over acidic catalysts by single step conversion for the production of diesel fuel and fuel blends. *Appl. Catal., B* **2015**, *174*, 383−394.
(34) Miao, C.; Marin-Flores, O.; Davidson, S. D.; Li, T.; Dong, T.; Gao, D.; Wang, Y.; Garcia-Pérez, M.; Chen, S. Hydrothermal catalytic deoxygenation of palmitic acid over nickel catalyst. *Fuel* **2016**, *166*, 302−308.
(35) Natewong, P.; Murakami, Y.; Tani, H.; Asami, K. Effect of Support Material on MgO-Based Catalyst for Production of New Hydrocarbon Bio-Diesel. *Am. Sci. Res. J. Eng. Technol. Sci.* **2016**, *22*, 153−165.
(36) Roh, H.-S.; Eum, I.-H.; Jeong, D.-W.; Yi, B. E.; Na, J.-G.; Ko, C. H. The effect of calcination temperature on the performance of $Ni/MgO-Al_2O_3$ catalysts for decarboxylation of oleic acid. *Catal. Today* **2011**, *164*, 457−460.
(37) Kubička, D.; Kaluža, L. Deoxygenation of vegetable oils over sulfided Ni, Mo and NiMo catalysts. *Appl. Catal., A* **2010**, *372*, 199−208.
(38) Taromi, A. A.; Kaliaguine, S. Green diesel production via continuous hydrotreatment of triglycerides over mesostructured γ-alumina supported NiMo/CoMo catalysts. *Fuel Process. Technol.* **2018**, *171*, 20−30.
(39) Morris, S. M.; Fulvio, P. F.; Jaroniec, M. Ordered mesoporous alumina-supported metal oxides. *J. Am. Chem. Soc.* **2008**, *130*, 15210−15216.
(40) Xu, B.; Xiao, T.; Yan, Z.; Sun, X.; Sloan, J.; González-Cortés, S. L.; Alshahrani, F.; Green, M. L. H. Synthesis of mesoporous alumina with highly thermal stability using glucose template in aqueous system. *Microporous Mesoporous Mater.* **2006**, *91*, 293−295.
(41) Peng, J.; Chen, P.; Lou, H.; Zheng, X. Catalytic upgrading of bio-oil by HZSM-5 in sub-and super-critical ethanol. *Bioresour. Technol.* **2009**, *100*, 3415−3418.
(42) Berteau, P.; Ceckiewicz, S.; Delmon, B. Role of the acid-base properties of aluminas, modified γ-alumina, and silica-alumina in 1-butanol dehydration. *Appl. Catal.* **1987**, *31*, 361−383.
(43) Rostom, S.; de Lasa, H. I. Propane Oxidative Dehydrogenation Using Consecutive Feed Injections and Fluidizable VOx/γAl2O3 and VOx/ZrO2−γAl2O3 Catalysts. *Ind. Eng. Chem. Res.* **2017**, *56*, 13109−13124.
(44) Charisiou, N. D.; Baklavaridis, A.; Papadakis, V. G.; Goula, M. A. Synthesis Gas Production via the Biogas Reforming Reaction Over $Ni/MgO-Al_2O_3$ and $Ni/CaO-Al_2O_3$ Catalysts. *Waste Biomass Valorization* **2016**, *7*, 725−736.
(45) Iriondo, A.; Barrio, V. L.; Cambra, J. F.; Arias, P. L.; Guemez, M. B.; Sanchez-Sanchez, M. C.; Navarro, R. M.; Fierro, J. L. G. Glycerol steam reforming over Ni catalysts supported on ceria and ceria-promoted alumina. *Int. J. Hydrogen Energy* **2010**, *35*, 11622−11633.
(46) Dou, B.; Wang, C.; Song, Y.; Chen, H.; Xu, Y. Activity of Ni−Cu−Al based catalyst for renewable hydrogen production from steam reforming of glycerol. *Energy Convers. Manage.* **2014**, *78*, 253−259.

DOI: 10.1021/acsomega.8b00562
ACS Omega 2018, 3, 7046−7060

(47) Sun, L.; Li, H.; Zhao, M.; Wang, G. High-performance lithium-sulfur batteries based on self-supporting graphene/carbon nanotube foam@ sulfur composite cathode and quasi-solid-state polymer electrolyte. *Chem. Eng. J.* **2018**, *332*, 8−15.
(48) Ma, X.; Cui, K.; Hao, W.; Ma, R.; Tian, Y.; Li, Y. Alumina supported molybdenum catalyst for lignin valorization: effect of reduction temperature. *Bioresour. Technol.* **2015**, *192*, 17−22.
(49) Ma, D.; Shu, Y.; Bao, X.; Xu, Y. Methane dehydroaromatization under nonoxidative conditions over Mo/HZSM-5 catalysts: EPR study of the Mo species on/in the HZSM-5 zeolite. *J. Catal.* **2000**, *189*, 314−325.
(50) Benitez, V. M.; Querini, C. A.; Fígoli, N. S. Characterization of WO_x/Al_2O_3 and MoO_x/Al_2O_3 catalysts and their activity and deactivation during skeletal isomerization of 1-butene. *Appl. Catal., A* **2003**, *252*, 427−436.
(51) Cordero, R. L.; Llambias, F. J. G.; Agudo, A. L. Temperature-programmed reduction and zeta potential studies of the structure of MoO_3/Al_2O_3 and MoO_3/SiO_2 catalysts effect of the impregnation pH and molybdenum loading. *Appl. Catal.* **1991**, *74*, 125−136.
(52) Wang, S.; Lu, G. Q. Reforming of methane with carbon dioxide over Ni/Al_2O_3 catalysts: effect of nickel precursor. *Appl. Catal., A* **1998**, *169*, 271−280.
(53) Chen, Y.-g.; Ren, J. Conversion of methane and carbon dioxide into synthesis gas over alumina-supported nickel catalysts. Effect of $Ni-Al_2O_3$ interactions. *Catal. Lett.* **1994**, *29*, 39−48.
(54) Scanlon, D. O.; Watson, G. W.; Payne, D. J.; Atkinson, G. R.; Egdell, R. G.; Law, D. S. L. Theoretical and experimental study of the electronic structures of MoO_3 and MoO_2. *J. Phys. Chem. C* **2010**, *114*, 4636−4645.
(55) Spevack, P. A.; McIntyre, N. S. Thermal reduction of molybdenum trioxide. *J. Phys. Chem.* **1992**, *96*, 9029−9035.
(56) Clayton, C. R.; Lu, Y. C. Electrochemical and XPS evidence of the aqueous formation of Mo_2O_5. *Surf. Interface Anal.* **1989**, *14*, 66−70.
(57) Baltrusaitis, J.; Mendoza-Sanchez, B.; Fernandez, V.; Veenstra, R.; Dukstiene, N.; Roberts, A.; Fairley, N. Generalized molybdenum oxide surface chemical state XPS determination via informed amorphous sample model. *Appl. Surf. Sci.* **2015**, *326*, 151−161.
(58) Hossain, M. Z.; Chowdhury, M. B. I.; Alsharari, Q.; Jhawar, A. K.; Charpentier, P. A. Effect of mesoporosity of bimetallic Ni-Ru-Al_2O_3 catalysts for hydrogen production during supercritical water gasification of glucose. *Fuel Process. Technol.* **2017**, *159*, 55−66.
(59) Hossain, M. Z.; Chowdhury, M. B. I.; Jhawar, A. K.; Charpentier, P. A. Supercritical water gasification of glucose using bimetallic aerogel Ru-Ni-Al_2O_3 catalyst for H_2 production. *Biomass Bioenergy* **2017**, *107*, 39−51.
(60) Youssef, E. A.; Chowdhury, M. B. I.; Nakhla, G.; Charpentier, P. Effect of nickel loading on hydrogen production and chemical oxygen demand (COD) destruction from glucose oxidation and gasification in supercritical water. *Int. J. Hydrogen Energy* **2010**, *35*, 5034−5042.
(61) Chowdhury, M. B. I.; Hossain, M. M.; Charpentier, P. A. Effect of supercritical water gasification treatment on Ni/La_2O_3-Al_2O_3-based catalysts. *Appl. Catal., A* **2011**, *405*, 84−92.
(62) Itthibenchapong, V.; Srifa, A.; Kaewmeesri, R.; Kidkhunthod, P.; Faungnawakij, K. Deoxygenation of palm kernel oil to jet fuel-like hydrocarbons using Ni-MoS_2/γ-Al_2O_3 catalysts. *Energy Convers. Manage.* **2017**, *134*, 188−196.
(63) Guzman, A.; Torres, J. E.; Prada, L. P.; Nuñez, M. L. Hydroprocessing of crude palm oil at pilot plant scale. *Catal. Today* **2010**, *156*, 38−43.
(64) Srifa, A.; Faungnawakij, K.; Itthibenchapong, V.; Viriya-Empikul, N.; Charinpanitkul, T.; Assabumrungrat, S. Production of bio-hydrogenated diesel by catalytic hydrotreating of palm oil over $NiMoS_2/\gamma$-Al_2O_3 catalyst. *Bioresour. Technol.* **2014**, *158*, 81−90.
(65) Bezergianni, S.; Dimitriadis, A.; Kalogianni, A.; Knudsen, K. G. Toward hydrotreating of waste cooking oil for biodiesel production. Effect of pressure, H_2/oil ratio, and liquid hourly space velocity. *Ind. Eng. Chem. Res.* **2011**, *50*, 3874−3879.
(66) Ford, J. P.; Immer, J. G.; Lamb, H. H. Palladium catalysts for fatty acid deoxygenation: influence of the support and fatty acid chain length on decarboxylation kinetics. *Top. Catal.* **2012**, *55*, 175−184.
(67) Rozmysłowicz, B.; Mäki-Arvela, P.; Tokarev, A.; Leino, A.-R.; Eränen, K.; Murzin, D. Y. Influence of hydrogen in catalytic deoxygenation of fatty acids and their derivatives over Pd/C. *Ind. Eng. Chem. Res.* **2012**, *51*, 8922−8927.
(68) Li, N.; Bi, Y.; Xia, X.; Chen, H.; Hu, J. Hydrodeoxygenation of Methyl Laurate over Ni Catalysts Supported on Hierarchical HZSM-5 Zeolite. *Catalysts* **2017**, *7*, 383.
(69) Ding, R.; Wu, Y.; Chen, Y.; Liang, J.; Liu, J.; Yang, M. Effective hydrodeoxygenation of palmitic acid to diesel-like hydrocarbons over MoO_2/CNTs catalyst. *Chem. Eng. Sci.* **2015**, *135*, 517−525.
(70) Méndez-Vilas, A. *Materials and Processes for Energy: Communicating Current Research and Technological Development*, 1st ed.; Formatex Research Center: Badajoz, Spain, 2013.
(71) Yang, L.; Ruess, G. L.; Carreon, M. A. Cu, Al and Ga based metal organic framework catalysts for the decarboxylation of oleic acid. *Catal. Sci. Technol.* **2015**, *5*, 2777−2782.
(72) Ahmadi, M.; Macias, E. E.; Jasinski, J. B.; Ratnasamy, P.; Carreon, M. A. Decarboxylation and further transformation of oleic acid over bifunctional, Pt/SAPO-11 catalyst and Pt/chloride Al 2 O 3 catalysts. *J. Mol. Catal. A: Chem.* **2014**, *386*, 14−19.
(73) Ahmadi, M.; Nambo, A.; Jasinski, J. B.; Ratnasamy, P.; Carreon, M. A. Decarboxylation of oleic acid over Pt catalysts supported on small-pore zeolites and hydrotalcite. *Catal. Sci. Technol.* **2015**, *5*, 380−388.
(74) http://www.engineeringtoolbox.com/fuels-higher-calorific-values-d_169.html (accessed on April 19, 2017).
(75) Jet fuel: ASTM D1655-15d, Diesel: Petro-Canada MSDS (accessed on April 19, **2017**).
(76) McKendry, P. Energy production from biomass (part 1): overview of biomass. *Bioresour. Technol.* **2002**, *83*, 37−46.
(77) The Official Site of the National Biodiesel Board. http://www.Biodiesel.org (accessed on April 19, 2017).
(78) Santillan-Jimenez, E.; Crocker, M. Catalytic deoxygenation of fatty acids and their derivatives to hydrocarbon fuels via decarboxylation/decarbonylation. *J. Chem. Technol. Biotechnol.* **2012**, *87*, 1041−1050.
(79) Effendi, A.; Zhang, Z.-G.; Hellgardt, K.; Honda, K.; Yoshida, T. Steam reforming of a clean model biogas over Ni/Al2O3 in fluidized- and fixed-bed reactors. *Catal. Today* **2002**, *77*, 181−189.
(80) Bibby, D. M.; McLellan, G. D.; Howe, R. F. Effects of Coke Formation and Removal on the Acidity of ZSM-5. *Stud. Surf. Sci. Catal.* **1987**, *34*, 651−658.
(81) McLellan, G. D.; Howe, R. F.; Parker, L. M.; Bibby, D. M. Effects of coke formation on the acidity of ZSM-5. *J. Catal.* **1986**, *99*, 486−491.
(82) Huang, X.; Liu, J.; Chen, J.; Xu, Y.; Shen, W. Mechanistic study of selective oxidation of dimethyl ether to formaldehyde over alumina-supported molybdenum oxide catalyst. *Catal. Lett.* **2006**, *108*, 79−86.
(83) Choudhury, M. B. I.; Ahmed, S.; Shalabi, M. A.; Inui, T. Preferential methanation of CO in a syngas involving CO_2 at lower temperature range. *Appl. Catal., A* **2006**, *314*, 47−53.
(84) Hossain, M. Z.; Jhawar, A. K.; Chowdhury, M. B. I.; Xu, W. Z.; Wu, W.; Hiscott, D. V.; Charpentier, P. A. Using subcritical water for decarboxylation of oleic acid into fuel range hydrocarbons. *Energy Fuels* **2017**, *31*, 4013−4023.
(85) Lu, Q.; Tang, Z.; Zhang, Y.; Zhu, X.-f. Catalytic upgrading of biomass fast pyrolysis vapors with Pd/SBA-15 catalysts. *Ind. Eng. Chem. Res.* **2010**, *49*, 2573−2580.
(86) Asikin-Mijan, N.; Lee, H. V.; Taufiq-Yap, Y. H.; Juan, J. C.; Rahman, N. A. Pyrolytic−deoxygenation of triglyceride via natural waste shell derived Ca(OH)2 nanocatalyst. *J. Anal. Appl. Pyrolysis* **2016**, *117*, 46−55.
(87) Romero, M. J. A.; Pizzi, A.; Toscano, G.; Bosio, B.; Arato, E. Study of an innovative process for the production of biofuels using non-edible vegetable oils. *Chem. Eng. Trans.* **2014**, *37*, 883−888.

DOI: 10.1021/acsomega.8b00562
ACS Omega 2018, 3, 7046−7060